Focused ultrasound-microbubble treatment arrests the growth and formation of cerebral cavernous malformations

Delaney G. Fisher[1], Tanya Cruz[1], Matthew R. Hoch[1], Khadijeh A. Sharifi[2,3], Ishaan M. Shah[1], Catherine M. Gorick [1], Victoria R. Breza[1], Anna C. Debski [1], Joshua D. Samuels [2], Jason P. Sheehan[3], David Schlesinger[4], David Moore[5], James W. Mandell[6], John R. Lukens [2], G. Wilson Miller[1,7], Petr Tvrdik [2,3] ✉ & Richard J. Price [1,7] ✉

Cerebral cavernous malformations (CCMs) are vascular lesions within the central nervous system that cause debilitating neurological symptoms. Currently, surgical excision and stereotactic radiosurgery, the primary treatment options, pose risks to some patients. Here we tested whether pulsed, low intensity, focused ultrasound-microbubble (FUS-MB) treatments control CCM growth and formation in a clinically representative *Krit1* null murine model. FUS-MB under magnetic resonance imaging (MRI) guidance opened the blood–brain barrier, with gadolinium contrast agent deposition most evident at perilesional boundaries. Longitudinal MRI revealed that, at 1 month after treatment, FUS-MB halted the growth of 94% of treated CCMs. In contrast, untreated CCMs grew ~7-fold in volume. FUS-MB-treated CCMs exhibited a marked reduction in *Krit1* null endothelial cells. In mice receiving multiple FUS-MB treatments with fixed peak-negative pressures, de novo CCM formation was reduced by 81%, indicating a prophylactic effect. Our findings support FUS-MB as a minimally invasive treatment modality that can safely arrest murine CCM growth and prevent de novo CCM formation in mice. If proven safe and effective in clinical trials, FUS-MB treatment may enhance therapeutic options for CCM patients.

Cerebral cavernous malformations (CCM) are vascular lesions originating in the capillary-venous vessels of the central nervous system[1]. These slow-flow vascular malformations are haemorrhage prone, grossly enlarged and lack many of the supporting cells of the neurovascular unit[2,3]. For patients with the familial form of the disease, multiple CCMs arise due to inherited mutations in one of the three CCM-related genes: *Krit1*, *CCM2* and *PDCD10* (refs. 1,4). In patients with the sporadic form of the disease, solitary lesions develop that frequently contain additional growth-promoting mutations in *PIK3CA*[5,6]. CCM patients can experience debilitating and life-altering symptoms such as motor and visual deficits, seizures and stroke[7]. These symptoms generally arise when CCMs bleed[8]. The current standard of care for CCM is invasive surgical resection. However, due to their eloquent location, CCMs in the brainstem are associated with risk of early morbidity and recurrent growth following incomplete resection[8-10]. Stereotactic radiosurgery is also a treatment option but conveys risks

[1]Department of Biomedical Engineering, University of Virginia, Charlottesville, VA, USA. [2]Department of Neuroscience, University of Virginia, Charlottesville, VA, USA. [3]Department of Neurological Surgery, University of Virginia Health System, Charlottesville, VA, USA. [4]Department of Radiation Oncology, University of Virginia Health System, Charlottesville, VA, USA. [5]Focused Ultrasound Foundation, Charlottesville, VA, USA. [6]Department of Pathology, University of Virginia, Charlottesville, VA, USA. [7]Department of Radiology and Medical Imaging, University of Virginia, Charlottesville, VA, USA. ✉e-mail: pt8bm.uva@gmail.com; rprice@virginia.edu
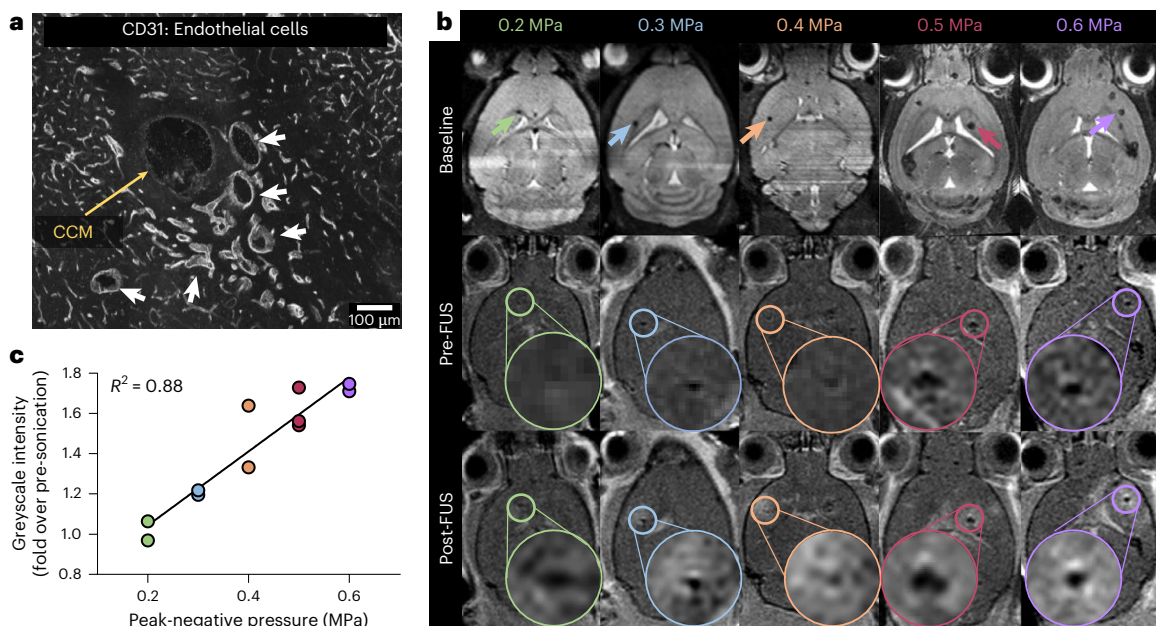
Fig. 1 | FUS-MB treatment opens the BBB within the CCM microenvironment. a, Confocal image of a CCM (in the absence of FUS) stained with CD31 for endothelial cells. Image depicts the grossly enlarged CCM core (yellow arrow) and moderately dilated perilesional vasculature (white arrows). **b**, Top row: baseline, high-resolution T2-weighted spin echo images used for selecting CCMs for FUS targeting. Arrowheads indicate selected CCMs. Middle row: T1-weighted spin echo images acquired following gadolinium contrast agent injection but immediately before FUS-MB application. Circles indicate targeted CCMs and insets display magnified views of the targeted CCMs. Bottom row: T1-weighted spin echo images acquired following gadolinium contrast agent injection and FUS application. Columns indicate PNPs used for sonication. T1 contrast enhancement is visible following FUS-MB treatment and localized to perilesional boundaries of the sonicated CCM. **c**, Line graph of T1 contrast enhancement as the fold change in greyscale intensity of sonicated CCMs in the post image over the pre image (as seen in **a**). Slope of linear regression is significantly different ($P < 0.0001$) from 0 by F-test.

associated with ionizing radiation that can lead to adverse radiation effects[11], including de novo lesion genesis[12]. Moreover, it is often unclear as to whether a CCM will regress, stabilize or progress[13–15]. Thus, CCM patients and parents of children with CCM, are put in the position of choosing between the risks of surgical intervention or inaction.

As an incisionless therapy with the ability to target eloquent brain locations, focused ultrasound (FUS) may represent an ideal alternative for CCM treatment. With targeting provided by magnetic resonance imaging (MRI), FUS delivers acoustic energy deep within the body to produce mechanical or thermal therapeutic effects[16]. When FUS is combined with an intravenous (i.v.) injection of gas-filled microbubbles (MBs), the oscillating pressure waves induce an alternating expansion and contraction of the gas within MBs, which in turn causes the MBs to push and pull on the walls of blood vessels. If performed in the brain, this procedure can induce a temporary opening of the blood–brain barrier (BBB). Detailed background on the safety of FUS-MB treatment is provided in recent comprehensive review articles[17,18].

FUS-MB treatment has been deployed primarily to enable enhanced delivery of drugs and other therapeutic agents into the brain for various neurological conditions[19–21]. However, FUS-MB has also been shown to be beneficial in the absence of drug delivery in pre-clinical models of Alzheimer's disease[22–27]. While the exact mechanism(s) behind the beneficial effect of FUS-MB in pre-clinical models of Alzheimer's disease are not completely understood, several clinical trials are testing the safety and feasibility of this approach in patients with Alzheimer's disease (NCT04118764, NCT04526262, NCT02986932, NCT03739905, NCT04250376). In this study, we tested whether FUS-MB could inhibit CCM growth and formation in *Krit1* null mice. After establishing that FUS-MB safely disrupts the BBB around CCMs, we determined that FUS-MB both halted the growth of virtually all treated CCMs and reduced *Krit1* null endothelial cells. Moreover, in mice receiving multiple fixed peak-negative pressure FUS-MB treatments, de novo CCM formation was also reduced.

In all, our findings support FUS-MB as a minimally invasive treatment modality that, in the absence of drug delivery, can therapeutically control the growth and de novo formation of CCMs.

Results

FUS-MB opens the BBB within the CCM microenvironment

Given the altered biomechanical properties[28–30] and increased calibre of the vasculature of CCMs and the surrounding perilesional vasculature (Fig. 1a), we first questioned whether FUS in combination with i.v. MB injection could effectively elicit BBB opening in CCM mice. We acquired baseline, high-resolution T2-weighted spin echo MR images of CCM mice to select CCMs for sonication. On the day of FUS treatment, gadolinium contrast agent (gadobenate dimeglumine, 1.058 kDa) was injected intravenously, and a pre-sonication T1-weighted spin echo MR image was obtained. We next performed FUS-MB on selected CCMs using peak-negative pressures (PNP), that is, ultrasound wave amplitudes, of 0.2–0.6 MPa and standard FUS parameters. FUS-MB clearly enhanced gadolinium delivery to CCMs, with more pronounced enhancement evident in the perilesional boundaries, as opposed to lesion cores (Fig. 1b). Gadolinium delivery, as assessed by the fold change in greyscale intensity above pre-sonication baseline, increased linearly with increasing PNP over the range of PNPs tested (0.2–0.6 MPa) (Fig. 1c). Thus, FUS-MB can effectively open the BBB within the CCM microenvironment, despite the enlarged and irregular microvasculature associated with the lesion.

FUS-MB does not acutely increase volume or bleeding of CCMs

Due to the propensity of CCMs to haemorrhage and the dysregulated state of the microvasculature in CCMs[1], we next sought to evaluate the safety of FUS-MB in this disease model. To determine whether growth or bleeding was acutely induced by FUS-MB at PNPs of 0.2–0.6 MPa, MR images of the brains of CCM mice were taken before and 24 h after FUS-MB. A three-dimensional (3D), T2-weighted spin echo sequence
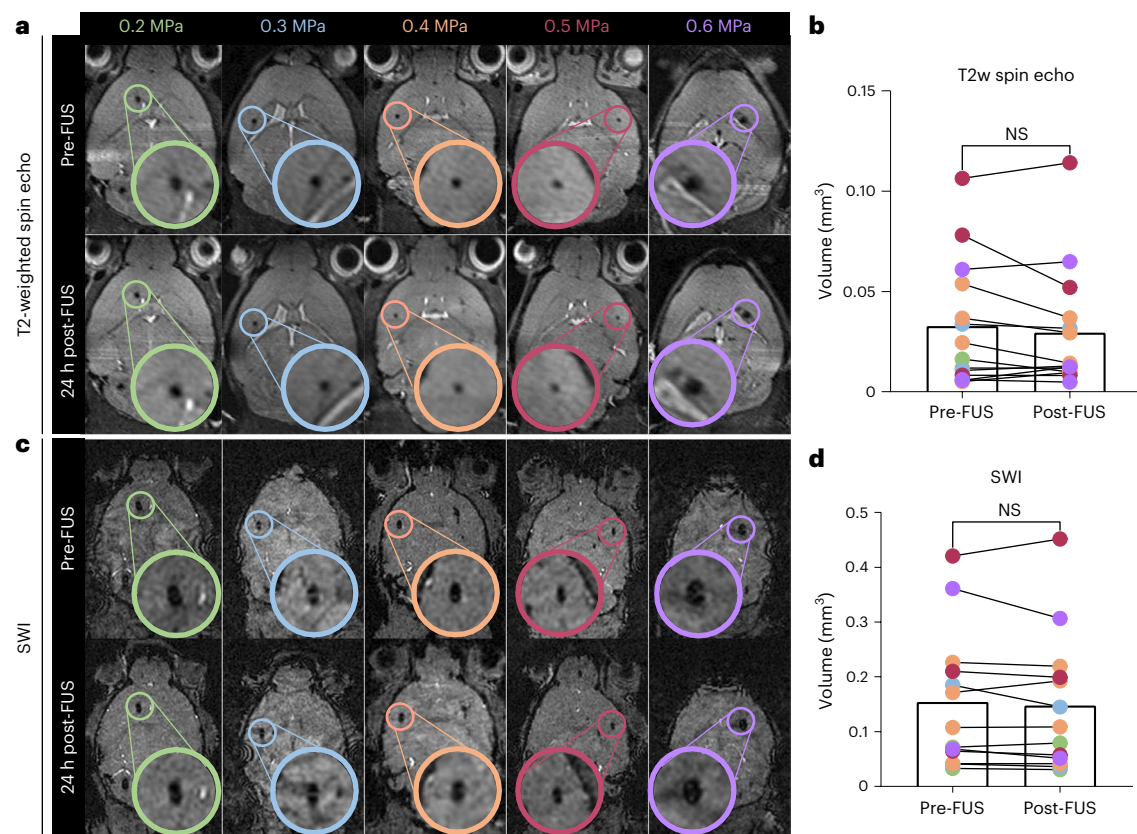
Fig. 2 | Acute stability of CCMs exposed to FUS-MB treatment. a, High-resolution T2-weighted spin echo images displaying either CCMs before sonication (top row) or 24 h following sonication (bottom row). Circles denote targeted CCMs and insets display magnified views of the targeted CCMs. **b**, Targeted CCM volumes before sonication and 24 h following sonication on T2-weighted spin echo images with colour indicating applied PNP. CCM volume does not significantly demonstrate changes in volume following sonication.

NS, not significant; $P = 0.41$; two-tailed Wilcoxon matched-pairs signed-rank test. **c**, High-resolution susceptibility-weighted images of the same mice in **a**, displaying either CCMs before sonication (top row) or 24 h following sonication (bottom row). **d**, Targeted CCM volumes before sonication and 24 h following sonication on susceptibility-weighted images with colour indicating applied PNP. CCM volume does not significantly demonstrate changes in bleeding following sonication. $P = 0.34$; two-tailed Wilcoxon matched-pairs signed-rank test.

was employed to accurately capture changes in CCM volume (Fig. 2a), while 3D susceptibility-weighted images (SWI) were acquired to capture changes in iron content and fluid flow (that is, bleeding or haemorrhage; Fig. 2c) with high sensitivity. Measurement of the hypointense lesion margins between pre- and post-sonication images revealed no evidence of growth or haemorrhage induced by FUS-MB (Fig. 2b,d), indicating that FUS-MB causes neither growth nor bleeding of CCMs at acute timepoints. Immunofluorescence staining of erythrocytes with Ter119 (Supplementary Fig. 1) confirmed that FUS-MB did not exacerbate lesion haemorrhage.

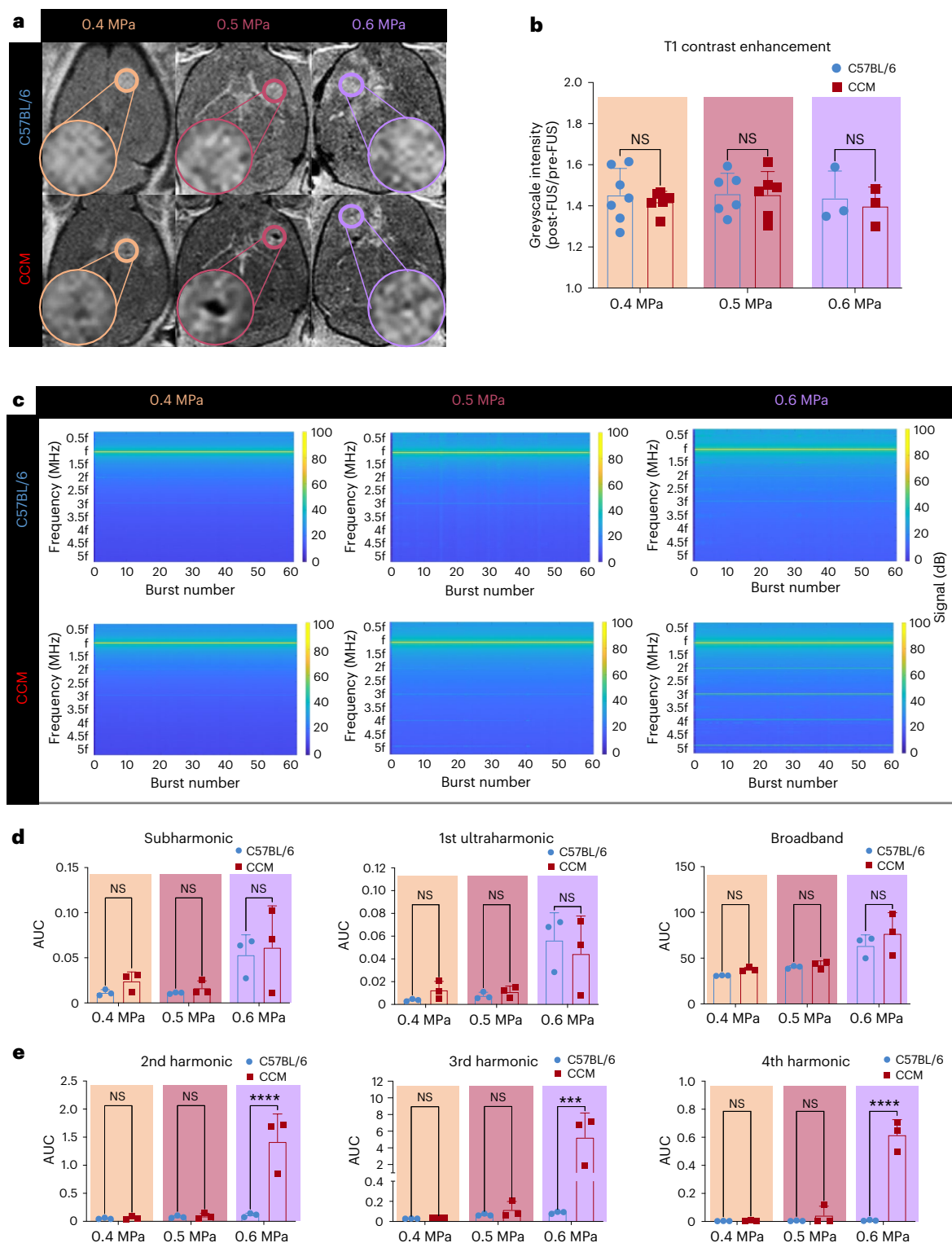### Comparison of FUS-MB responses between C57BL/6 and CCM mice

To test whether CCM mice differentially respond to FUS-MB at PNPs of 0.4–0.6 MPa, we compared T1 contrast enhancement (indicative of the degree of BBB opening and contrast delivery) and passive cavitation detection (PCD) measurements (indicative of the MB activity during sonication) between non-transgenic (C57BL/6) and CCM mice. Our analysis revealed no significant differences in T1 contrast enhancement between C57BL/6 and CCM mice at any of the tested PNPs (Fig. 3a,b), suggesting that the extent of BBB opening is comparable. To compare the MB activity, spectrograms of the frequency response for each burst during the FUS application were generated (Fig. 3c), and cavitation levels were quantified for spectra signifying unstable and stable MB activity (Fig. 3d,e). Spectral domains associated with a transition towards or an increase in unstable, inertial cavitation of MBs (that is, subharmonic, ultraharmonics and broadband)[31,32] increased with PNP and were comparable between C57BL/6 and CCM mice (Fig. 3d). Spectral domains associated with stable cavitation (that is, harmonics)[32,33] were comparable for PNPs of 0.4 MPa and 0.5 MPa (Fig. 3e). However, at a PNP of 0.6 MPa, CCM mice displayed an increase in harmonic emissions, while the harmonic emissions of C57BL/6 mice remained similar to that observed at lower PNPs (Fig. 3e). Altogether, these results suggest that FUS-MB affects C57BL/6 and CCM mice similarly with regards to the degree of BBB opening and MB activity induced, particularly unstable MB activity. Meanwhile, at high PNPs, stable MB activity is enhanced in CCM mice, albeit without comparable increases in unstable, inertial cavitation.

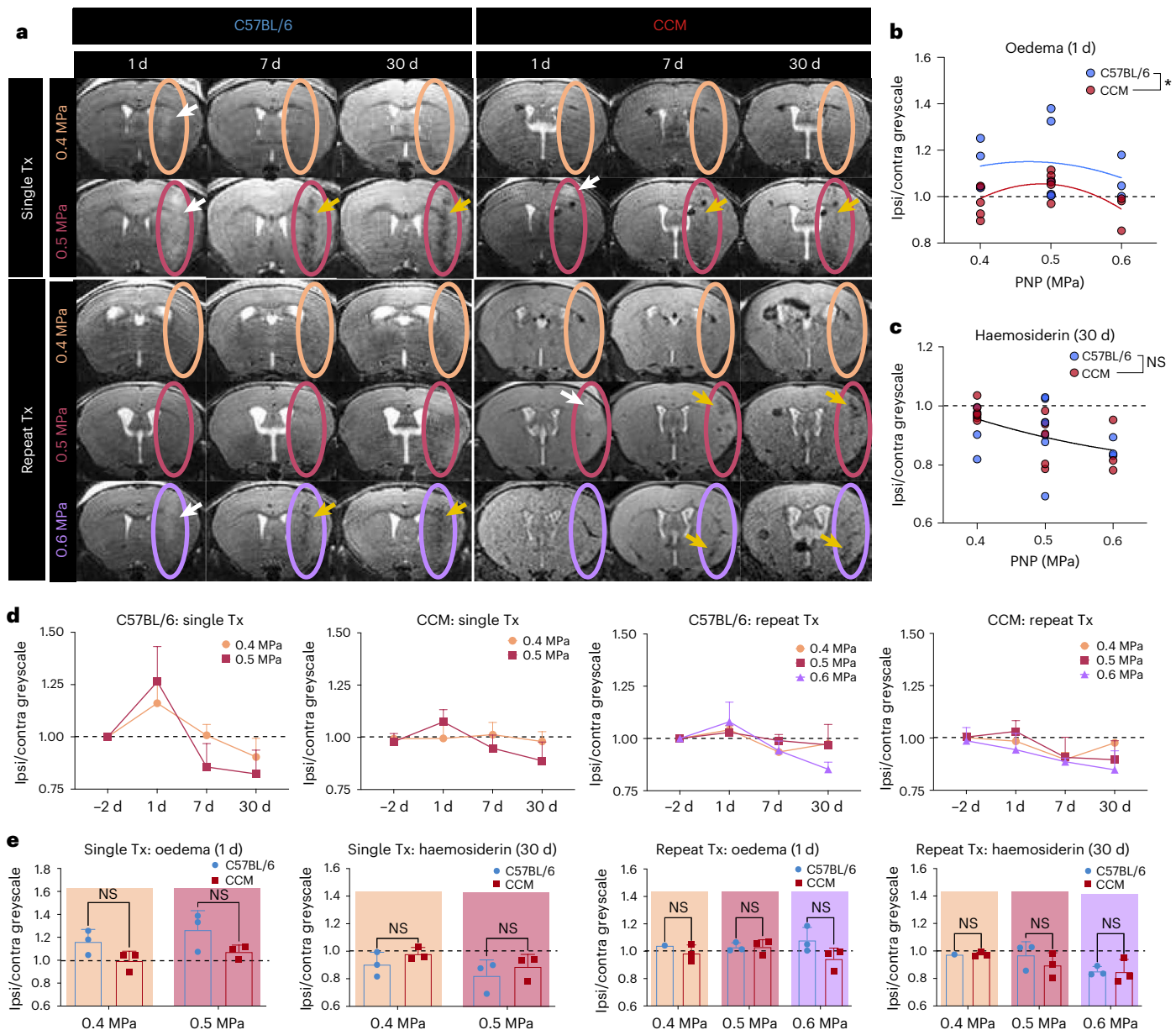### CCM mice are not differentially sensitive to FUS-MB

To assess the longitudinal safety of FUS-MB in CCM mice, we collected T2-weighted spin echo sequences over a 1-month period following FUS-MB in C57BL/6 and CCM mice (Fig. 4a). Different FUS-MB regimens were tested: a single FUS-MB application or repeat applications performed three times for PNPs of 0.4 MPa or two times for PNPs of 0.5 MPa and 0.6 MPa, with a 3-day spacing between sonications. Oedema, visible as hyperintensity on T2-weighted MRI, was apparent in lesion-free brain tissue in a fraction of both C57BL/6 and CCM mice at 1 day post FUS-MB for PNPs of 0.5 MPa and 0.6 MPa (Fig. 4a,b). Haemosiderin deposits, visible as hypointensity on T2-weighted MRI, were also apparent in lesion-free brain tissue in C57BL/6 and CCM mice at timepoints beyond 1 day post FUS-MB and persisted for at least 1 month following FUS-MB for PNPs of 0.5 MPa and 0.6 MPa (Fig. 4a,c).

Fig. 3 | Comparison of FUS-MB treatment contrast enhancement and acoustic emission signatures between C57BL/6 and CCM mice. a, Representative T1-weighted spin echo images acquired following gadolinium contrast agent injection and FUS-MB in C57BL/6 mice or CCM mice for PNPs of 0.4–0.6 MPa. **b**, Bar graph of T1 contrast enhancement. Data are means ± s.d. Enhancement is comparable in C57BL/6 (n = 7, 6 and 3 mice for 0.4, 0.5 and 0.6 MPa, respectively) and CCM (n = 6, 6 and 3 mice for 0.4, 0.5 and 0.6 MPa, respectively) mice for PNPs of 0.4–0.6 MPa. P = 0.92 for 0.4 MPa, P = 0.9998 for 0.5 MPa and P = 0.96 for 0.6 MPa; two-way analysis of variance (ANOVA) with Šidák's multiple comparison test. **c**, Spectrograms of the frequency response for each burst during the FUS-MB application averaged over cohorts of C57BL/6 and CCM mice at PNPs

of 0.4–0.6 MPa (n = 3 mice per group and 2–3 sonication replicates per mouse). **d**, Subharmonic, first ultraharmonic and broadband emissions for C57BL/6 (n = 3 per group) and CCM (n = 3 per group) mice at PNPs of 0.4–0.6 MPa. Data are means ± s.d. P > 0.4 for all PNPs; two-way ANOVA with Šidák's multiple comparisons test. **e**, Second, third and fourth harmonic emissions for C57BL/6 (n = 3 per group) and CCM (n = 3 per group) mice at PNPs of 0.4–0.6 MPa. Data are means ± s.d. Stable cavitation-associated signatures between C57BL/6 and CCM mice are comparable at 0.4 MPa and 0.5 MPa, but significantly increased in CCM mice at 0.6 MPa. P > 0.7 for 0.4–0.5 MPa and 2nd–4th harmonics; ****P < 0.0001, ***P = 0.0006 and ****P < 0.0001 for 0.6 MPa and 2nd, 3rd and 4th harmonics, respectively; two-way ANOVA with Šidák's multiple comparisons test.

Fig. 4 | CCM mice are not differentially sensitive to adverse effects generated by FUS-MB treatment at high PNPs. a, Representative high-resolution, T2-weighted spin echo images of C57BL/6 and CCM mice at 1, 7 and 30 days post sonication at PNPs of 0.4–0.6 MPa in either a single sonication (Tx) or repeat sonication treatment regimen. Ovals denote focal column. White arrows denote hyperintensities associated with oedema. Yellow arrows denote hypointensities associated with haemosiderin deposition. **b**, Scatterplot of ipsilateral-to-contralateral greyscale intensity at 1 day post FUS (when oedema is visible) of C57BL/6 and CCM mice for PNPs of 0.4–0.6 MPa. *P = 0.047; comparison of fits with F-test for a 2nd-order polynomial regression. **c**, Scatterplot of ipsilateral-to-contralateral greyscale intensity at 30 days post FUS (when haemosiderin is visible) of C57BL/6 and CCM mice for PNPs of 0.4–0.6 MPa. P = 0.77; comparison of fits with F-test for a 2nd-order polynomial regression. **d**, Line graphs of

ipsilateral-to-contralateral greyscale intensities over the 1-month imaging period for all PNPs within a mouse model and treatment arm. Oedema on day 1 is generally followed by haemosiderin on days 7 and 30. n = 3 for all groups. Data are means ± s.d. **e**, Ipsilateral-to-contralateral greyscale intensities over the 1-month imaging period for all PNPs within a mouse model and treatment arm, indicating no significant differences when comparing models at individual PNPs within a treatment arm. n = 3 for all groups. Data are means ± s.d. P = 0.1368 and P = 0.5386 for both PNPs in the single treatment arm for oedema and haemosiderin, respectively; P > 0.7 for PNPs of 0.4 MPa and 0.5 MPa, and P = 0.0923 for PNP of 0.6 MPa in the repeat treatment arm for oedema; P > 0.5 for all PNPs in the repeat treatment arm for haemosiderin; two-way ANOVA with Holm–Šidák's multiple comparisons test.

Oedema, quantified by an increase in the ipsilateral-to-contralateral greyscale ratio, primarily occurred after FUS-MB with PNPs of 0.5 MPa (Fig. 4b), and haemosiderin deposition, quantified by a decrease in the ipsilateral-to-contralateral greyscale ratio, increased as a function of PNP (Fig. 4c). Generally, acute oedema was associated with chronic haemosiderin deposition for both models and both treatment arms (Fig. 4d). When comparing the prevalence of oedema and haemosiderin deposition between C57BL/6 and CCM mice for each treatment regimen

and PNP, no significant differences were seen (Fig. 4e). However, when treatment regimens were aggregated, C57BL/6 mice actually exhibited a greater propensity for oedema than CCM mice (Fig. 4b), yet C57BL/6 and CCM mice shared an equivalent correlation for haemosiderin deposition (Fig. 4c). These results suggest that, while FUS-MB with PNPs greater than 0.4 MPa are safe for CCMs, FUS-MB at increased PNPs can induce oedema and haemosiderin deposition, consistent with that seen in C57BL/6 mice.
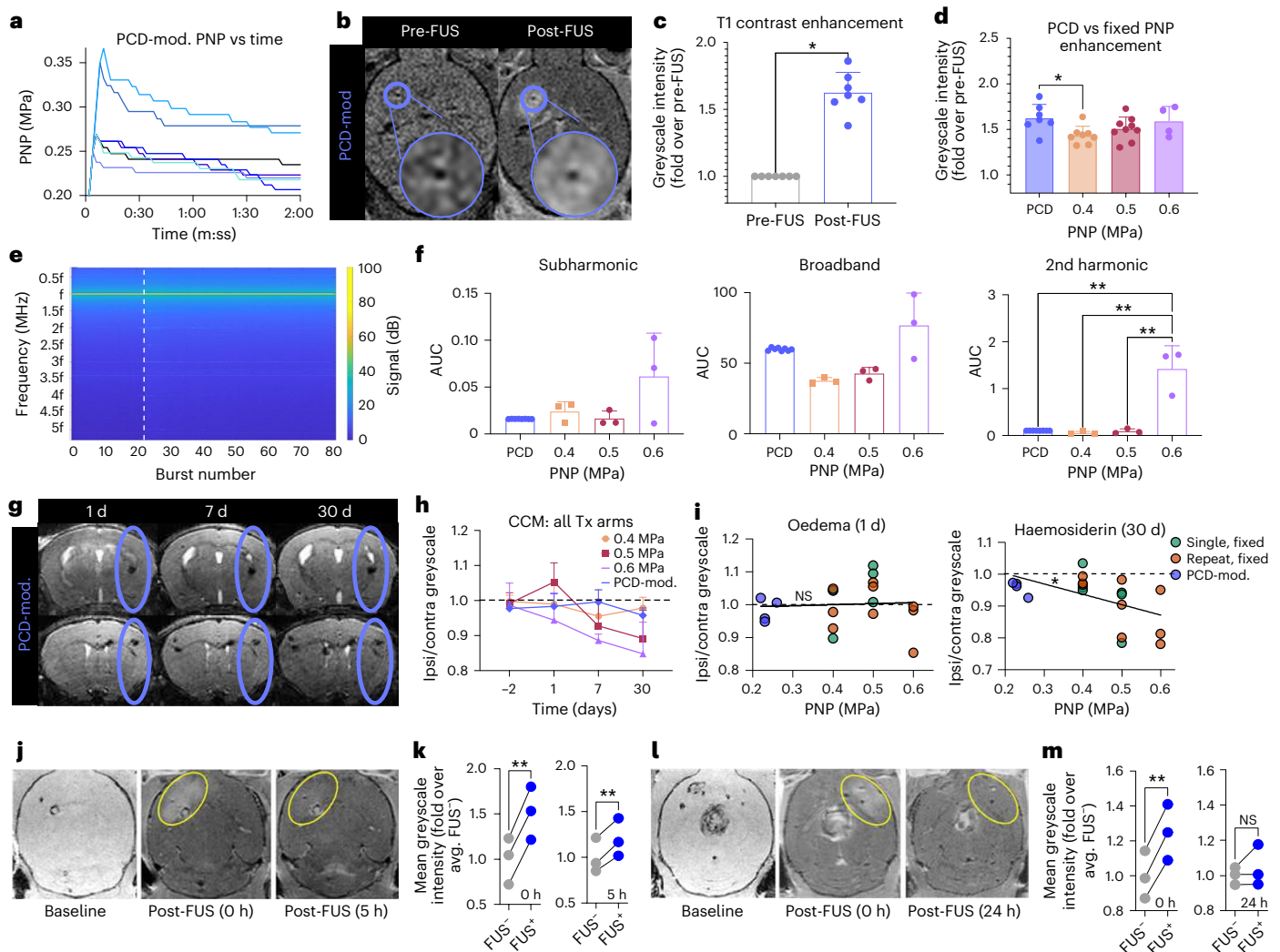
Fig. 5 | Real-time PCD modulation of PNP ensures the safety of sonicated brain tissue without compromising gadolinium delivery. a, Applied PNP versus time during PCD feedback-controlled approach. Each line indicates the average applied PNP across two sonication targets for the same mouse during a single FUS sonication period. **b**, Representative T1-weighted contrast images before and after FUS-MB with PCD-modulated PNPs. **c**, T1 contrast enhancement as the fold change in greyscale intensity of sonicated CCMs in the post image over the pre image. *n* = 7. Data are means ± s.d. *P = 0.016; two-tailed Wilcoxon matched-pairs signed-rank test. **d**, T1 contrast enhancement as the fold change in greyscale intensity of sonicated CCMs in the post image over the pre image for CCM mice. Data are means ± s.d. *n* = 7, 8, 9 and 4 for PCD, 0.4 MPa, 0.5 MPa and 0.6 MPa groups, respectively. *P = 0.0293; one-way ANOVA with Dunnett's multiple comparison's test. **e**, Spectrogram of the frequency response for each burst during the FUS application averaged over CCM mice with PCD-modulated PNP (*n* = 4 mice and 2 sonication replicates per mouse). Dotted line indicates time of microbubble injection. **f**, Acoustic emissions for CCM mice. Data are means ± s.d. *n* = 8, 3, 3 and 3 for PCD, 0.4 MPa, 0.5 MPa and 0.6 MPa groups, respectively. **P = 0.003 for all comparisons; two-way ANOVA with Šidák's multiple comparisons test. **g**, Representative T2-weighted spin echo images of CCM mice at 1, 7 and 30 days post sonication with PCD-modulated PNP. **h**, Line

graphs of ipsilateral-to-contralateral greyscale intensities over the 1-month imaging period for CCM mice and all PNP regimens. *n* = 6, 6, 3 and 4 for 0.4 MPa, 0.5 MPa, 0.6 MPa and PCD-mod groups, respectively. Data are means ± s.d. **i**, Scatterplot of ipsilateral-to-contralateral greyscale intensity versus time-averaged PNP for CCM with single treatments and fixed PNP, repeat treatments and fixed PNP, or repeat treatments and PCD-modulated PNP mice on day 1 (left) or day 30 post FUS (right). For oedema, there is no correlation. *P = 0.0163 for haemosiderin; linear regression with *F*-test. **j**–**m**, BBB opening duration in CCM mice after FUS-MB treatment with PCD-modulated PNP. **j**, Representative high-resolution T2-weighted baseline (left; 24 h pre FUS), low-resolution T1 contrast (middle; immediately post FUS) and high-resolution T1 RARE (right; 5 h post FUS) MRIs. Yellow outline denotes FUS application region. **k**, Contrast enhancement immediately post FUS (left; **P = 0.0025) and 5 h post FUS (right; **P = 0.0092). *n* = 3 per group. Two-tailed paired *t*-tests. **l**, Representative high-resolution T2-weighted baseline (left; 24 h pre FUS), low-resolution T1 contrast (middle; immediately post FUS) and high-resolution T1 RARE (right; 24 h post FUS) MRIs. Yellow outline denotes FUS application region. **m**, Contrast enhancement immediately post FUS (left; **P = 0.0039) and 24 h post FUS (right; *P* = 0.4136). *n* = 3 per group. Two-tailed paired *t*-tests.

PCD-modulated FUS-MB safely enhances contrast in CCMs

To ensure safety of our FUS-MB application and examine the effect of more clinically representative FUS-MB regimens in CCM mice, we performed FUS-MB using a real-time PCD feedback control system to modulate the applied PNP during sonication[34–36]. Using this PCD-modulated PNP approach, the maximum PNP occurred within

the first 15 s of treatment, and the PNP generally decreased gradually over the sonication period (Fig. 5a). This approach resulted in a time-averaged PNP ranging from 0.23 MPa to 0.30 MPa and a maximum PNP ranging from 0.25 MPa to 0.38 MP. PCD-modulated PNPs successfully increased T1 contrast enhancement in the CCM microenvironment (Fig. 5b,c). Comparing PCD modulation of PNP to
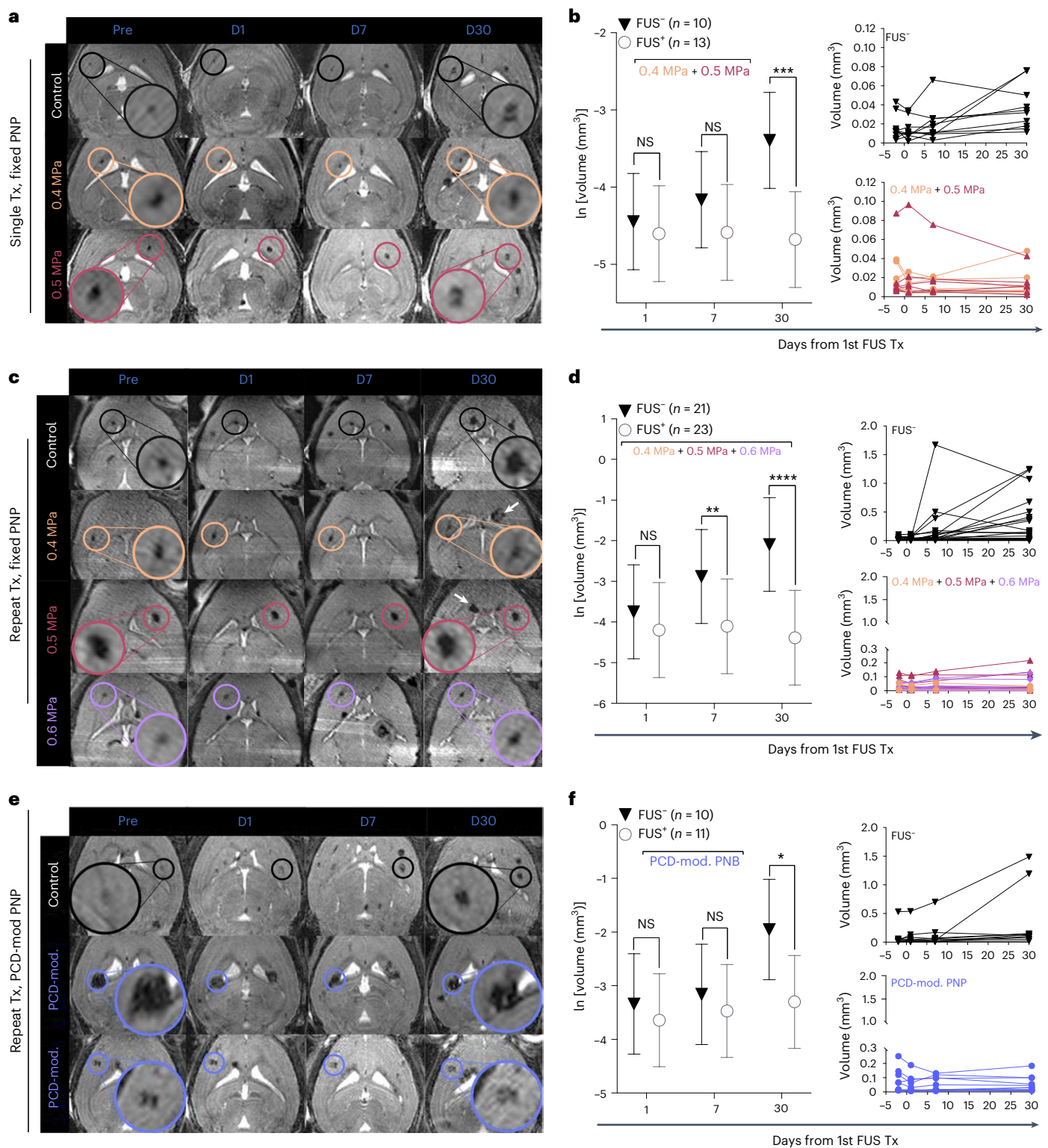
Fig. 6 | FUS-MB treatment arrests the growth of CCMs. a,c,e, Longitudinal T2-weighted spin echo images for representative mice in the (**a**) single sonication with fixed PNP arm, (**c**) repeat sonication with fixed PNP arm or (**e**) repeat sonication with PCD-modulated PNP arm. Black circles indicate non-sonicated control lesions and coloured circles indicate sonicated lesions corresponding to PNP applied. White arrows denote new lesions formed in non-sonicated hemisphere. **b,d,f,** Left: summary plots comparing the natural log transform of CCM volume between sonicated CCMs and non-sonicated CCMs for mice in the (**b**) single sonication with fixed PNP arm, (**d**) repeat sonication with fixed PNP

arm or (**f**) repeat sonication with PCD-modulated PNP arm. Data are means ± s.d. Right: line graphs of CCM volume for individual CCMs for each treatment group. At 30 days, sonicated CCMs are significantly smaller than non-sonicated control CCMs for all treatment arms. ***$P = 0.0002$, ****$P < 0.0001$ and *$P = 0.0131$ for the single fixed PNP, repeat fixed PNP and repeat PCD-mod. PNP arms, respectively; linear mixed-effect model and pairwise comparison with Tukey's adjustment. At 7 days, sonicated CCMs are significantly smaller than non-sonicated CCMs in the repeat FUS and fixed PNP arm. **$P = 0.0021$, linear mixed-effect model and pairwise comparison with Tukey's adjustment.
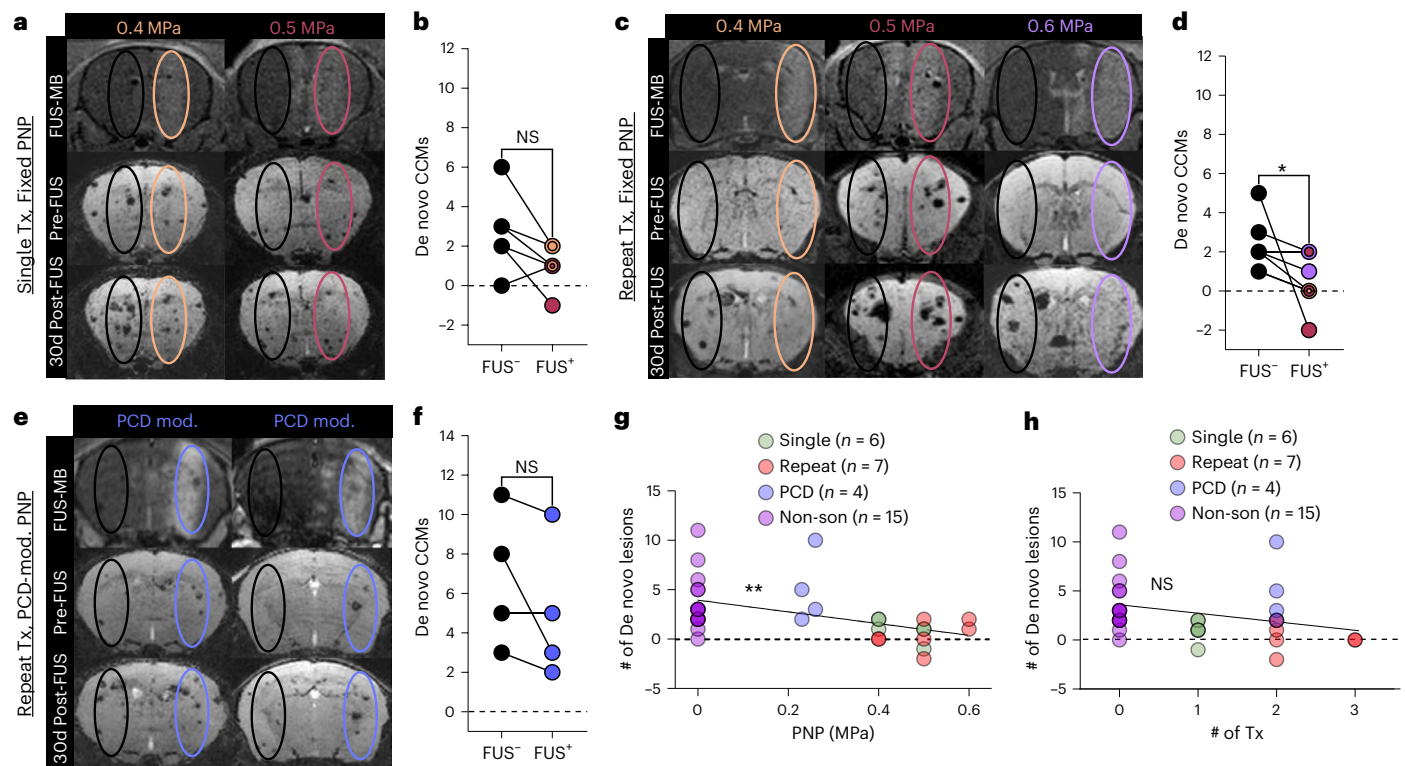
Fig. 7 | FUS-MB treatment with fixed PNP and repeat sonications can prevent de novo lesion formation. a,c,e, Top rows: T1-weighted spin echo images taken immediately following FUS-MB treatment with hyperintense signal denoting the focal column. Middle and bottom rows: minimum intensity projection images of longitudinal T2-weighted spin echo images to visualize through 1 mm of the focal column for representative mice in the (**a**) single sonication with fixed PNP arm, (**c**) repeat sonication with fixed PNP arm or (**e**) repeat sonication with PCD-modulated PNP arm. Black ovals denote contralateral non-sonicated ROIs for de novo quantification, while coloured ovals represent sonicated ROIs. **b,d,f**, Paired line graphs comparing the change in CCM number 1 month following FUS-MB between the sonicated brain region and the contralateral non-sonicated brain region for mice in the (**b**) single sonication with fixed PNP arm

(n = 6 CCM mice), (**d**) repeat sonication with fixed PNP arm (n = 6 CCM mice) or (**f**) repeat sonication with PCD-modulated PNP arm (n = 4 CCM mice). Concentric circles indicate multiple mice with the same number of de novo CCMs. Colours indicate applied PNP. For mice receiving the repeat FUS regimen with fixed PNP, the number of new lesions formed in the sonicated brain region is significantly reduced compared with the contralateral brain region. *P = 0.0312; two-tailed Wilcoxon matched-pairs signed-rank test. **g**, Plot of de novo CCM formation and PNP for all treatment conditions. **P = 0.0064; linear regression indicates that de novo CCM formation and PNP are inversely correlated. **h**, Plot of de novo CCM formation and number of FUS applications (that is, # of Tx) for all treatment conditions. P = 0.0914; linear regression indicates that de novo CCM formation and # of Tx are not inversely correlated.

the fixed PNP approach revealed that PCD-modulated PNP resulted in T1 contrast enhancement levels that were higher than those achieved with a fixed PNP of 0.4 MPa and similar to those achieved with fixed PNPs of 0.5 MPa and 0.6 MPa (Fig. 5d). Acoustic emissions measurements revealed that PCD-modulated PNP elicits comparable subharmonic, broadband and harmonic spectra when compared to fixed PNPs of 0.4 MPa and 0.5 MPa (Fig. 5e,f). Longitudinal T2-weighted MRI also demonstrated that PCD-modulated PNP obviates oedema and haemosiderin deposition following FUS-MB (Fig. 5g,h). For FUS-MB in CCM mice, oedema was comparable across PNPs and a reduction of haemosiderin deposition was seen with PNPs averaging less than or equal to 0.4 MPa (Fig. 5i). Tissue sections from day 30 CCM mice that received PCD-modulated FUS-MB treatment were stained with H&E (Supplementary Fig. 2). Sections were examined by a neuropathologist (J.W.M.) who noted no obvious qualitative differences in CCMs and surrounding tissue when comparing FUS-MB-treated hemispheres and contralateral hemispheres. We also performed studies to ascertain the approximate duration of BBB opening after FUS-MB treatment using PCD-modulated PNP in CCM mice. Our results indicate that, while the BBB is still open to gadolinium contrast agent at 5 h after PCD-modulated FUS-MB treatment, it is nearly closed at 24 h (Fig. 5j–m). This duration of BBB opening is consistent with previous studies performed on both rodents[37–39] and humans[40–42], suggesting that the *Krit1* mutation phenotype does not adversely affect the ability

of the BBB to recover after PCD-modulated FUS-MB treatment. Altogether, these data indicate that PCD modulation of PNP ensures the safety of FUS-MB in CCM brain tissue and elicits enhanced gadolinium delivery compared with fixed PNPs.

FUS-MB treatment arrests CCM growth

We then asked whether FUS-MB stimulates therapeutically beneficial responses for CCMs. First, we tested several FUS-MB regimens for their ability to control the growth of CCMs. CCM mice were placed in (1) a single FUS-MB regimen with fixed PNP (that is, one FUS-MB treatment at either 0.4 MPa or 0.5 MPa), (2) a repeat FUS-MB regimen with fixed PNP (that is, three FUS-MB treatments at 0.4 MPa or two FUS-MB treatments at 0.5 MPa or 0.6 MPa, all staged 3 days apart) or (3) a repeat FUS-MB regimen with PCD-modulated PNP (that is, two FUS-MB treatments staged 3 days apart). Mice were treated between 2 and 3 months of age, a period of rapidly escalating lesion burden[43]. Male and female mice across 9 litters were used (Supplementary Table 1), and MR images were acquired following each sonication and up to 1 month thereafter (Fig. 6a,c,e). Sonicated CCM volumes were compared to non-sonicated CCMs of similar baseline size and anatomical location within the same cohort of mice. The average sonicated and non-sonicated CCM volume before FUS-MB application was 0.039 mm³ for both conditions. Remarkably, CCMs exposed to FUS-MB in all treatment regimens exhibited nearly complete cessation of growth (Fig. 6b,d,f). Only 3 of 47

CCMs exposed to FUS-MB grew more than 0.02 mm^3 in 1 month, while 26 of 41 CCMs not exposed to FUS-MB grew this amount in the same period. Significant differences in lesion volume between the sonicated and non-sonicated CCMs were seen after 30 days for all treatment arms (Fig. 6b,d,f). At 7 days, sonicated CCMs were significantly smaller than non-sonicated CCMs in the repeat FUS-MB and fixed PNP arm (Fig. 6d). At 30 days post FUS-MB, sonicated CCMs in all treatment arms demonstrated a markedly reduced mean lesion volume, reaching just 28%, 10% and 26% of the mean volume of the non-sonicated CCM volume in the single fixed PNP, repeat fixed PNP and repeat PCD-modulated PNP arms, respectively. Increases in PNP and number of FUS-MB treatments were both inversely correlated with increased lesion volume (Supplementary Fig. 3a,b). The effect of sex on CCM volume and FUS-MB was also evaluated (Supplementary Fig. 4a,b). After 30 days, CCMs in male mice were larger than those in female mice, regardless of FUS-MB treatment (Supplementary Fig. 4a and Table 2). However, sex did not affect the ability of FUS-MB to control CCM growth (Supplementary Fig. 4a and Table 2).

FUS-MB can prevent de novo lesion formation

To then ascertain whether FUS-MB impacts the formation of new lesions, we counted the number of lesions contained within the focal zone (that is, T1-contrast-enhanced brain region) in MR images taken before FUS-MB, as well as 1 month following FUS-MB. The same analysis was performed in the contralateral hemisphere of each mouse using the same volume and mirrored anatomical location (Fig. 7a,c,e). The change in the number of lesions from the pre image to the 30-days post-FUS-MB image was compared for the sonicated and contralateral brain areas within each mouse. This analysis revealed that the repeat FUS-MB regimen with fixed PNP significantly reduced the formation of new CCMs by 81% compared with the contralateral brain region (Fig. 7d). While the single FUS-MB with fixed PNP regimen and repeat FUS-MB with PCD-modulated PNP regimen did not significantly reduce de novo CCM formation (Fig. 7b,f), incorporating these data into an analysis comparing PNP level to de novo lesion formation did reveal a statistically significant inverse correlation (Fig. 7g). This suggests that the potential for reducing de novo CCM formation with FUS-MB treatment may be enhanced at higher applied energy levels. Interestingly, in contrast to PNP level, the number of FUS-MB treatments did not correlate with de novo lesion formation (Fig. 7h). Importantly, in all treatment arms, FUS-MB did not induce an increase in lesion formation. In fact, both the single and repeat FUS-MB with fixed PNP cohorts contained one mouse that displayed fewer lesions in the sonicated brain region 1 month following FUS-MB compared with the pre image, suggesting that some CCMs may be cleared with FUS-MB. The effect of sex on de novo CCMs and FUS-MB was also evaluated (Supplementary Fig. 4c,d). Sex did not significantly alter the ability of FUS-MB to control CCM formation (Supplementary Fig. 4c and Table 2).

FUS-MB reduces *Krit1* null endothelium in CCMs

To elucidate how FUS-MB may halt CCM growth and prevent new lesion formation, we performed an extensive immunohistological analysis of brain sections at 1, 7 or 30 days post FUS-MB. We first questioned whether FUS-MB affects the *Krit1* null endothelium. After the induction of endothelial *Krit1* knockout (*Krit1*[KO]) in our CCM mouse model, tdTomato is expressed via the PC::G5-tdT lineage reporter[44], allowing visualization of the *Krit1*[KO] cells (Fig. 8a). Others have also used similar systems to track clonally expanding endothelial cells in CCMs before[2,45]. In non-sonicated lesions, *Krit1*[KO] endothelial cells were hypertrophic, rounded and highly disorganized (Fig. 8b). *Krit1*[KO] endothelial cell area was comparable between sonicated and non-sonicated lesions at 1 and 7 days post FUS-MB. However, at 30 days post FUS-MB, the *Krit1*[KO] staining pattern underwent a striking change marked by the adoption of thin and elongated (that is, more prototypically endothelial) morphologies (Fig. 8a). The average area of *Krit1*[KO] endothelium was also significantly reduced (Fig. 8b); however, there was no change in the proliferation of *Krit1*[KO] cells (Supplementary Fig. 5a,b), which may indicate that FUS-MB does not affect clonal expansion of *Krit1*[KO] cells. We also examined the expression of a mesenchymal endothelial cell marker (alpha smooth muscle actin, SMA) in *Krit1*[KO] endothelial cells in and around CCMs at day 30 (Supplementary Fig. 6). The fraction of *Krit1*[KO] endothelium that was SMA[+] was unchanged for FUS-MB treated (PCD-modulated) CCMs when compared to control CCMs, consistent with FUS-MB treatment having no detectable influence on endothelial-to-mesenchymal transition.

FUS-MB remodels the immune landscape in CCMs

Because FUS-MB is thought to augment microglial phagocytosis[46,47], we also looked for evidence of enhanced microglia/macrophage phagocytic activity in sonicated lesions, with particular emphasis on the potential for clearance of erythrocytes. At 1 day post FUS-MB, the number of Iba1^{+} cells (microglia/macrophages) was significantly decreased in sonicated lesions (Fig. 8c,d); however, their average area was significantly increased (Fig. 8c,e,f). Closer examination revealed these enlarged Iba1^{+} cells as macrophages (Fig. 8f). Unexpectedly, the number of cells expressing the phagolysosomal marker CD68 was actually decreased at 1 day and 7 days in sonicated lesions (Fig. 8g). Further, the percent of red blood cells (Ter119^{+}) co-localized with Iba1^{+} cells, which would be suggestive of phagocytosis of erythrocytes, was not increased by FUS-MB. In fact, this metric was actually decreased at 7 days after FUS-MB (Fig. 8h). Interestingly, the CD68^{+} cell population steadily recovered after the acute reduction by FUS-MB (Fig. 8g). The proliferation of Iba1^{+} cells and the proliferation, number and size of GFAP[+] astrocytes were not significantly different between sonicated and non-sonicated lesions at any timepoint following FUS-MB (Supplementary Fig. 5a,c–g). Finally, we found that CD45^{+} immune cell infiltration was significantly elevated at 7 days post FUS-MB in sonicated lesions (Supplementary Fig. 7a,b). Because CD45^{+} cells are thought to

Fig. 8 | FUS-MB treatment restores endothelial morphology to the mutated CCM vasculature and remodels CCM immune landscape. a, Immunofluorescence images of non-sonicated and sonicated CCMs at 30 d post FUS-MB with staining for mutated vasculature (*Krit1*[KO]), microglia/macrophages (Iba1) and erythrocytes (Ter119). **b**, Graph of average *Krit1*[KO] area at 1, 7 and 30 days post FUS-MB for non-sonicated and sonicated CCMs, indicating reduced area in sonicated CCMs at 30 days. *$P = 0.0199$; linear mixed-effect model and pairwise comparison with Tukey's adjustment. **c**, Immunofluorescence images of non-sonicated and sonicated CCMs at 1 and 7 d post FUS-MB with staining for mutated vasculature (*Krit1*[KO]), microglia/macrophages (Iba1) and proliferation (Ki67). **d**, Graph of density of microglia/macrophages at 1, 7 and 30 days post FUS-MB for non-sonicated and sonicated CCMs, revealing a reduced number in sonicated lesions at 1 day. ***$P = 0.0003$; linear mixed-effects model and pairwise comparison with Tukey's adjustment. **e**, Graph of the natural log of the average microglia/macrophage area at 1, 7 and 30 days post FUS-MB for non-sonicated and sonicated CCMs, demonstrating an increase in microglia/macrophage

size in sonicated lesions at 1 day. *$P = 0.0106$; linear mixed-effect model and pairwise comparison with Tukey's adjustment. **f**, Immunofluorescence images of non-sonicated and sonicated CCMs at 1 day post FUS-MB with staining for mutated vasculature (*Krit1*[KO]), microglia/macrophages (Iba1), lysosomes (CD68) and erythrocytes (Ter119). Insets display ×63 maximum intensity projections of the corresponding ×20 image. Arrows denote macrophages. **g**, Graph of the natural log of phagocyte density at 1, 7 and 30 days post FUS-MB for non-sonicated and sonicated CCMs, revealing a reduced number in sonicated lesions at 1 day. ***$P = 0.0009$; linear mixed-effects model and pairwise comparison with Tukey's adjustment. **h**, Graph of the natural log of the percent of erythrocytes co-localized in microglia/macrophages at 1, 7 and 30 days post FUS-MB for non-sonicated and sonicated CCMs, indicating a smaller amount in sonicated lesions at 7 days. *$P = 0.0303$; linear mixed-effects model and pairwise comparison with Tukey's adjustment. Data are means ± s.d. (**b,d,e,g,h**). For FUS[−], $n = 13, 37$ and 24 CCMs at 1, 7 and 30 days, respectively. For FUS[+], $n = 40, 42$ and 35 CCMs at 1, 7 and 30 days, respectively.

drive lesion progression, the potential significance of their enhanced presence in FUS-MB stabilized lesions warrants future investigation. Inspecting the morphology and location of CD45^{+}, Iba1^{+} and *Krit1*[KO] signal revealed monocytes in the lumens of lesions, Iba1^{+} microglia/macrophage processes extending to CD45^{+} immune cells and CD45^{+}Iba1^{+} cells lining mutated vessels (Supplementary Fig. 7a).

Clinical FUS systems are equipped to treat CCMs in patients
Finally, to assess the feasibility of clinical CCM treatments with FUS-MB, we designed FUS-MB treatment plans for 3 CCM patients who chose to have their lesions treated with stereotactic radiosurgery

(SRS)[11] (Supplementary Fig. 8). SRS treatment plans are shown in Supplementary Fig. 8a, with 12.5 Gy and 6.3 Gy isodose lines circumscribing the target CCM and its margin. We reimagined these treatment plans for FUS-MB using the NaviFUS clinical MRI-guided FUS system (Supplementary Fig. 8b). These CCMs in eloquent brain locations were accessible for FUS-MB treatment. A total of 43 sonication points spanning 2 cm in diameter and 8.65 cm³ in volume provided adequate coverage of the target CCM in all 3 patients. Thus, we demonstrate that current clinical FUS systems are equipped to treat CCMs in patients, especially those who may not be good candidates for traditional surgical excision.
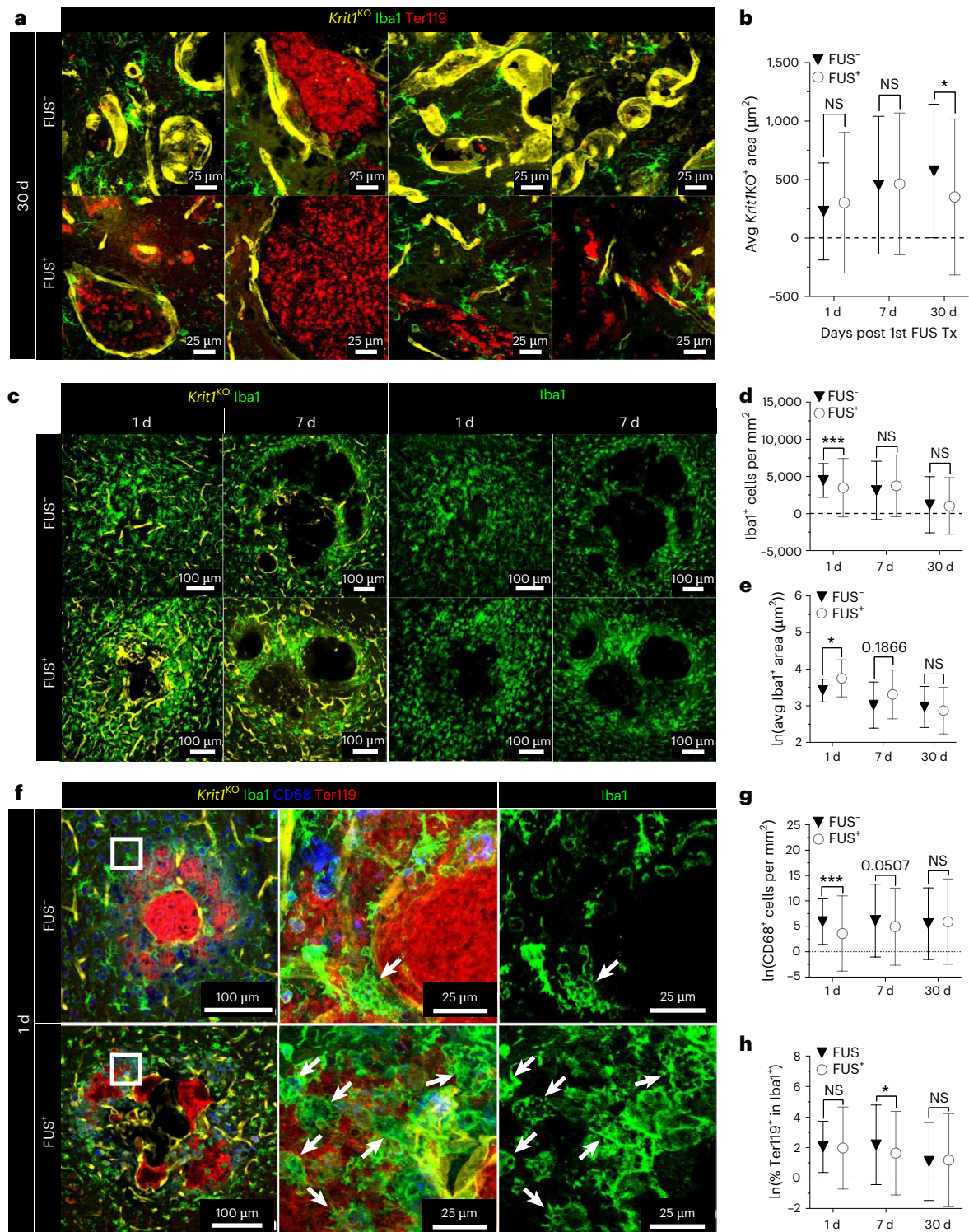
Discussion

Patients with CCM can sustain incapacitating and even life-threatening neurological symptoms. The only current curative treatment option for these patients is resection of symptomatic CCMs via invasive surgery, which is associated with a high risk of post-operative morbidities for lesions located in eloquent regions. While SRS may be deployed for some patients, SRS can present adverse radiation side effects, induce new CCMs in certain patient populations and may have limited therapeutic efficacy[48–59]. Concurrently, FUS-MB is now well known to exert potentially favourable bioeffects[19,27]. Indeed, we demonstrate here that FUS-MB can elicit powerful therapeutic effects in a clinically representative murine model of CCM. At the cellular level, CCMs exposed to FUS-MB exhibited a reduction in *Krit1* null endothelium and a remodelled immune landscape. As an incisionless therapy with the ability to target eloquent brain locations, FUS-MB is a technology that could radically transform how CCMs are treated.

One key consideration in these studies was whether FUS-MB signatures in CCM mice differ from those in non-transgenic mice. Since the vasculature associated with CCMs is known to be irregular and dilated[3,60], the effectiveness of FUS-MB had the potential to be reduced or otherwise altered. Increased vessel diameters could reduce the interaction between the oscillating MBs and vessel walls[61,62]. Moreover, the slow flow rate in the lesion core could reduce the number of MBs accumulating within the CCM[60]. Our studies indicate that the pattern of T1 contrast enhancement is localized to the perilesional boundaries of the CCM, which may indicate that the lesion core is not substantially interacting with MBs, perhaps due to its grossly enlarged diameter or its slow flow rate. Meanwhile, the perilesional microvasculature displayed marked gadolinium accumulation regardless of moderate vessel diameter dilation compared with normal brain capillaries. Further, our findings suggest that T1 contrast enhancement as well as subharmonic, ultraharmonic and broadband acoustic signatures of MB activity are not significantly different between CCM mice and C57BL/6 mice. While the harmonic signatures for PNPs of 0.4 MPa and 0.5 MPa were not significantly different between CCM and C57BL/6 mice, increases in harmonic signatures were seen in CCM mice at 0.6 MPa. This is the only indication that the altered properties of the CCM vasculature, such as vessel diameter, stiffness and contractility[28–30], can impact MB activity when high enough PNPs are applied. In addition, since CCMs have a baseline leakiness, it was possible that FUS-MB would not increase the accumulation of small molecules within the lesion microenvironment. Nevertheless, T1 contrast enhancement from the post-FUS image over the pre-FUS image is indeed apparent for PNPs ranging from 0.3 MPa to 0.6 MPa, indicating that gadolinium accumulation is increased over baseline levels via FUS-MB. Ultimately, while the pattern of T1 contrast enhancement may be altered in CCM mice, FUS-MB treatment still effectively opens the BBB in the perilesional vasculature of the lesion, and the MRI and acoustic signatures are largely comparable to those in C57BL/6 mice.

The capricious state of these haemorrhage-prone CCMs raised an important concern: would FUS-MB increase the propensity of CCMs to bleed? The addition of mechanical stress and disruption of already loose endothelial cell tight junctions from oscillating MBs had the potential to weaken the stability of CCMs. We did not provide an assessment of increased or decreased bleeding in the treated lesions using a standard histological approach such as Perls stain, which is an important consideration for future studies. However, our findings using other approaches do corroborate the safety of FUS-MB for CCMs. Susceptibility-weighted images, which have an increased sensitivity to blood products, demonstrated no acute changes in bleeding between the pre- and post-sonication images. T2-weighted spin echo sequences, which can accurately represent lesion volume and internal architecture[43], displayed no acute changes in lesion volume between the pre- and post-sonication images. These results also continued

for post-sonication images at later timepoints of up to 1 month, indicating that FUS-MB is safe for CCMs both acutely and chronically. Meanwhile, our results did indicate that oedema and haemosiderin deposits can be seen in lesion-free brain tissue in both C57BL/6 and CCM mice when using PNPs greater than 0.4 MPa. This finding further supports the use of PCD-modulated PNP feedback systems that have been widely adopted in clinical trials to ensure the safety of FUS-MB treatments[31,33–36,63].

After testing the safety of FUS-MB treatment, we questioned whether it could be therapeutic for CCMs. From analysis of longitudinal MR images, we show that FUS-MB is capable of fully arresting the growth of pre-existing CCMs. Notably, this CCM stabilization effect occurred across multiple litters and for both sexes. Interestingly, untreated CCMs in male mice grew faster than those in female mice, suggesting that sex influences lesion progression in this model, a topic that warrants further investigation. Comparing our results to those from other energy-deposition therapies, specifically SRS and laser interstitial thermal therapy (LITT), is informative. We can make comparisons between our results and clinical studies wherein individual CCM volumes have been measured both before and after targeted therapy. For SRS, a meta-review reports that 97.7% of 303 total patients across 8 studies exhibited either lesion regression or stabilization[64]. FUS-MB treatment in mice was comparable, eliciting stabilization or regression in 94% of treated lesions. Nevertheless, one potential advantage of FUS-MB over SRS is its non-ionizing nature. With FUS-MB, the adverse radiation effects observed in 11% of SRS patients[11] would be obviated. In addition, familial CCM patients could be treated without generating de novo lesions, which can be a concern for SRS[12]. For LITT, a meta-review reports that average lesion size decreases by 59% with treatment[65]. While FUS-MB treatment did not reduce average lesion size to this degree in mice, CCMs in two mice were eradicated (that is, no longer visible on MRI), indicating that responses of this magnitude may be achievable. One potential advantage of FUS-MB over LITT is that it does not cause significant heating, the measurement and control of which may be difficult when treating CCMs[66]. Moreover, while LITT is minimally invasive, it does require placing a probe in the lesion under MRI guidance. In contrast, FUS-MB requires only an intravenous MB injection and does not involve a skull burr hole.

It is also important to view the potential of the FUS-MB approach for treating patients with cavernous angioma with symptomatic haemorrhage (CASH)[67], as this is the population that most commonly requires treatment. The MRI methods deployed in this study cannot discern which CCMs had haemorrhaged before FUS-MB treatment, a scenario that could simulate CASH in patients. Pre-screening mice with quantitative susceptibility mapping MRI to identify CCMs with recent bleeds[68,69] could potentially discern whether FUS-MB treatment differentially affects CASH-like lesions. However, we emphasize that the overwhelming majority (94%) of CCMs in this study were completely stabilized by FUS-MB; therefore, the presence of a differentially responsive subset of lesions is unlikely. In any event, larger CCM lesions exhibiting bleeding or growth are more likely to rebleed and grow than smaller stable lesions[70]. FUS-MB could provide a minimally invasive alternative to stabilize such large lesions without the risks associated with surgery or the lack of intervention. We do also note that MRIs used to identify and track lesions were not directly correlated with histology, so we could not assess whether individual treated lesions were primordial or multicavernous. Testing whether FUS-MB differentially affects primordial vs multicavernous lesions is an important topic for future investigation.

Further, FUS-MB treatment could introduce new options for patients with the familial form of the disease. Familial CCM patients have multiple lesions, of which several can often arise in locations that are inoperable or are associated with a very high risk for post-operative morbidities[8,13]. FUS-MB could be used to stabilize multiple CCMs within

a single treatment session, including those in eloquent locations. Our results also suggest that FUS-MB may prevent de novo CCM formation, so treated regions may be protected from future CCMs. Nevertheless, future studies would be needed to determine how to best apply FUS-MB treatment to prevent new CCMs from forming, with subsequent validation in clinical trials for familial patients.

The ability of FUS-MB to exert powerful therapeutic effects for CCMs was surprising; however, this is not the first disease indication wherein FUS-MB has been shown to be protective. FUS-MB—in the absence of drug delivery—has also exhibited a therapeutic effect in pre-clinical models of Alzheimer's disease[22–27]. The exact mechanism of action remains unclear, although many studies have investigated the potential mechanisms behind its benefit[23–26,71].

In this study, our extensive histological analysis lends some insight into how FUS-MB may benefit CCMs. At 1 month post FUS-MB, when growth control is evident for all FUS-MB regimens, the amount of *Krit1* null endothelium per lesion was substantially reduced, despite no change in cell proliferation. In addition, FUS-MB treatment converted *Krit1* null endothelium from a rounded and disorganized morphology into one characterized by a sparse and wispy appearance. Thus, we hypothesize that FUS-MB-mediated arrest of CCM is at least partially due to morphological changes in *Krit1* null endothelial cells, which are the genesis of the disease.

Because FUS-MB increases phagocytosis in other disease contexts[46,47], another hypothesis for CCM stabilization was that FUS-MB-exposed microglia and macrophages would become activated and phagocytose erythrocytes. However, our data are not consistent with this putative mechanism of lesion control. Instead, we found that the co-localization of Iba1+ microglia/macrophages with erythrocytes was actually decreased at 7 days post FUS-MB. Beyond microglia and macrophages, numerous studies indicate that FUS-MB increases immune cell infiltration in a variety of disease states[19,47,72–75]. Consistent with these studies, we confirmed that FUS-MB increases overall immune cell (CD45+) infiltration in CCMs, signifying an altered immune landscape as a potential mechanism for CCM stabilization. Ultimately, several mechanisms may underlie the protective role of FUS-MB for CCM. Going forward, an important line of future investigation will entail identifying more refined hypotheses for the mechanism(s) through which the FUS-MB treatment leads to CCM stabilization and prevention, followed by testing of these hypotheses through reductionist approaches.

So far, no pharmacological agent has been approved for the treatment of CCM, yet a few drugs have entered clinical trials (propranolol: NCT03589014, REC-994: NCT05085561, simvastatin: NCT01764451, and atorvastatin: NCT02603328). In addition, many drugs for CCM are being examined in the pre-clinical stage[1]. These drug candidates have the potential to integrate with the FUS-MB approach used in this study, especially since surgically inaccessible CCMs in eloquent regions are accessible for FUS-MB using current clinical FUS systems. It may be possible to inject therapeutic agents at the time of FUS-MB treatment to better localize them to the CCM microenvironment. In particular, FUS-MB may be able to enhance the delivery of larger molecular weight biologics, such as antibodies and gene therapies, that would have a greater potential to accumulate in the CCM microenvironment with the aid of increased permeability via FUS-MB treatment[19,20,76]. Our current results indicating that FUS-MB treatment can stabilize CCMs support further investigation into the potential for this approach to also elicit therapeutic delivery.

Methods

Animals
All animal experiments were approved by the University of Virginia Animal Care and Use Committee. Mice were housed under standard laboratory conditions (22 °C and 12 h/12 h light/dark cycle). The CCM mouse models used here (*Pdgfb-CreERT2;Krit1*[fl/null] or

Cdh5-CreERT2;Krit1[fl/null]) harbour biallelic deletions of the *Krit1* gene, which is the CCM gene most commonly mutated in patients with the familial form of the disease. Further, the mouse model yields multiple CCMs throughout the brain, consistent with presentation of familial disease in humans[43]. Mouse model generation has been described previously[43]. In addition, these experimental animals also carried the reporter allele PC::G5-tdT[44], which expresses the fluorescent marker tdTomato specifically in *Krit1* null cells following Cre recombination. On postnatal day 5, *Krit1* gene ablation was induced with an injection of tamoxifen (subcutaneous, 50 μl at 2 mg ml^{-1} in corn oil). Genotypes were confirmed by Transnetyx. Non-transgenic control mice in this study were C57BL/6 (Charles River). All mice were treated between 9 weeks and 13 weeks of age. Mouse sex, litter, age and treatment assignment are listed in detail in Supplementary Table 1.

MR imaging
MR imaging was performed using either a 7 T Bruker/Siemens ClinScan or a 9.4 T Bruker BioSpec small animal MRI scanner. T2-weighted spin echo images were acquired at 7 T with the Siemens 3D T2-SPACE sequence (repetition time of 3,000 ms, echo time of 80 ms, voxel size of 125 μm × 125 μm × 100 μm, 2 averages and 20-min acquisition time) or at 9.4 T with the Bruker 3D T2-TurboRARE sequence (repetition time of 2,000 ms, echo time of 55 ms, turbo factor of 18, voxel size of 125 μm × 125 μm × 125 μm, 1 average and 30-min acquisition time). Susceptibility-weighted images were acquired only at 7 T (repetition time of 18 ms, echo time of 10 ms, voxel size of 130 μm × 130 μm × 130 μm, 2 averages and 15-min acquisition time). T1-weighted spin echo images were acquired at 9.4 T with the Bruker 2D T1-RARE sequence (repetition time of 1,500 ms, echo time of 6 s, voxel size of 156 μm × 156 μm × 350 μm, 1 average and 3-min acquisition time). All imaging was performed under isoflurane anaesthesia, and body temperature was maintained with a heated, circulating water bed.

Selection of CCMs for sonication
Following baseline MR image acquisition, images were reviewed to assess appropriate CCMs for sonication. CCMs located within the left or right striatum, corpus callosum or cerebral cortex were eligible for targeting. The average sonicated and non-sonicated (contralateral control) CCM volume before FUS application was 0.039 mm^3 for both conditions in the longitudinal studies. Before safety evaluation measurements and analysis, sonications were confined to single CCMs without neighbouring CCMs located dorsally or ventrally that would be within the focal zone. Following the initial safety evaluation, multiple CCMs were eligible for sonication if they were within the same focal volume.

FUS-MB treatment
FUS-MB treatment was performed with the RK-300 small bore FUS device (FUS Instruments). Heads of mice were shaved and depilated before supine placement and coupling to the transducer with degassed ultrasound gel. FUS-MB was performed with a 1.13 MHz single-element transducer using a 10-ms burst length over a 2,000-ms period for 60 total sonications during a 2-min sonication duration. Fixed PNP application was performed using the 'Burst' mode on the FUS Instruments software. PCD-modulated PNP was performed using the 'Blood–brain barrier' mode of the FUS Instruments software. Parameters used for this feedback control system included a starting pressure of 0.2 MPa, pressure increment of 0.05 MPa, maximum pressure of 0.4 MPa, 20 sonication baselines without MBs, area under the curve (AUC) bandwidth of 500 Hz, AUC threshold of 10 standard deviations, pressure drop of 0.95, and frequency selection of the subharmonic, first ultraharmonic and second ultraharmonic. Gadolinium contrast agent (Multihance) was injected as a bolus intravenously with a dose of 0.01 mmol diluted in saline at a molarity of 0.2 mmol ml^{-1} before T1-RARE image acquisition.

Albumin-shelled MBs were made in-house as previously described[77] and intravenously injected as a bolus dose of 10^5 MBs per gram body weight. Distribution of MB diameter and concentration was acquired with a Coulter counter (Multisizer 3, Beckman Coulter) before sonication. High-resolution T2-weighted images and T1-RARE images were used to guide FUS targeting to the pre-selected CCM. A single sonication target was used in all experiments, except in the case of PCD-modulated PNPs, in which two sonication targets were used. Mice receiving the repeat FUS-MB regimens had all sonications staged 3 days apart with the same anatomical location targeted each time.

Acoustic signatures from passive cavitation detection
Acoustic emissions were detected with a fibre-optic hydrophone (Precision Acoustics) of 10-mm diameter and 15-mm aperture centre-mounted within the ultrasound transducer. Emissions data were processed and spectrograms were generated with a custom MATLAB script. The AUC of the acoustic emissions at the subharmonic (0.5f) and ultraharmonics (1.5f, 2.5f) were calculated after applying a 300-Hz bandwidth filter. Broadband emissions were evaluated by summing acoustic emissions following the removal of all emissions at the fundamental frequency (f), harmonics (2f, 3f, 4f), subharmonic (0.5f) and ultraharmonics (1.5f, 2.5f, 3.5f).

T1 contrast enhancement analysis
Gadolinium accumulation following FUS-MB was evaluated using the enhancement of T1 contrast in T1-RARE images. In a DICOM viewer (Horos Project), a region of interest (ROI) was drawn around the boundaries of the enhanced (hyperintense) region on the image slice containing the targeted lesion. The ROI was then copied onto the pre-sonication T1-RARE image on the same slice. For C57BL/6 mice, ROIs were drawn around the boundaries of the enhanced (hyperintense) region in similar ventral/dorsal slice depths as for CCM mice. Mean greyscale intensity for each ROI was recorded, and fold change in greyscale intensity from the post image to the pre image was calculated. This process was repeated for all sonicated mice across each PNP.

BBB closure time after FUS-MB treatment
Target selection and FUS-MB treatment using PCD-modulated feedback proceeded as previously described, except that BBB opening was confirmed immediately after treatment with a lower-resolution 2D-RARE MRI sequence (repetition time of 1,500 ms, echo time of 5.5 ms, voxel size of 156 μm × 156 μm × 400 μm, 1 average and 6-min 25-s acquisition time). Mice were then allowed to recover. Next, at either 5 h or 24 h after FUS-MB treatment, mice were anaesthetized with inhaled isoflurane, Multihance was injected (0.2 mmol ml^{-1}), and high-resolution T1-RARE MRIs were acquired to ascertain whether the BBB was still open at these later timepoints. T1 contrast enhancement analysis proceeded as previously described to yield mean greyscale intensity for FUS$^+$ and contralateral FUS$^-$ ROIs. For each post-FUS-MB treatment timepoint, all datapoints are reported as fold change over average FUS$^-$ greyscale intensity.

Brain tissue oedema and haemosiderin deposition analysis
Oedema and haemosiderin deposition in lesion-free brain tissue following FUS-MB were evaluated in 3D Slicer using the high-resolution T2-weighted spin echo MR images. MR images were initially segmented by the brain tissue boundaries to generate a mask of the brain. Bias field correction was then applied with the N4ITK MRI Bias Field Correction tool in 3D Slicer to correct for inhomogeneities in signal intensity across the brain due to mouse rotation relative to the MR surface coil. Mean greyscale intensity was then recorded within ROIs of equal volume in lesion-free brain tissue for both non-sonicated (contralateral) and sonicated (ipsilateral) hemispheres on the same dorsal slice. Healthy brain tissue would have an ipsilateral-to-contralateral greyscale ratio near 1. Oedema would produce a ratio greater than 1, while haemosiderin would produce a ratio less than 1.

CCM growth analysis
CCM volume before, and longitudinally following, FUS-MB was evaluated in Horos using the high-resolution T2-weighted spin echo MR images. For each timepoint, an ROI was manually drawn around the sonicated CCM in each slice it was present. The Horos 'Compute Volume' tool was then used to calculate the 3D volume of the CCM across imaging timepoints. In the same mice, ROIs were also drawn around non-sonicated CCMs (that is, control CCMs) that had similar volumes and anatomical locations as sonicated lesions. CCM mice with enlarged ventricles, a rare but potential co-morbidity of this model, at the 1-month timepoint were removed from this analysis.

New lesion formation analysis
Formation of new CCMs was assessed by calculating the change in lesion number from the baseline pre-FUS to the 1-month post-FUS high-resolution T2-weighted spin echo MR images. For both timepoints, an ROI was first drawn around the T1 contrast enhanced boundaries within the T1-RARE images taken following FUS-MB, extending from the most dorsal to the most ventral slices of the brain and focal column. These ROIs were copied onto the T2-weighted spin echo images and adjusted to match the same anatomical positioning. These ROIs were then copied to the contralateral brain region and adjusted to mirror the same anatomical positioning. CCMs within the ROIs were then manually counted and recorded for both timepoints and for both the ipsilateral ROI and the contralateral ROI. The baseline CCM number was subtracted from the 1-month CCM number for both the ipsilateral and contralateral ROI volumes in each mouse to produce the number of new CCMs formed in each ROI volume during the 1-month time period. CCM mice with enlarged ventricles at the 1-month timepoint were removed from this analysis.

Immunohistochemistry and histology
Mice were perfused with phosphate-buffered saline (PBS) and 4% para-formaldehyde, and after collection, brains were fixed overnight in 4% paraformaldehyde and dehydrated in 30% sucrose solution for 24 h. Brains were then embedded in Optimal Cutting Temperature Compound (TissueTek) for cryosectioning at 30-μm thickness. Sections were incubated in blocking solution (1% bovine serum albumin, 2% normal donkey serum, 0.1% Triton X-100 and 0.05% Tween-20 in PBS) for 2 h at r.t. Brain sections were then incubated with goat anti-CD31 (1:20, R&D Systems, AF3628), rat anti-GFAP-Alexa Fluor 488 (1:50, eBioscience, 53-9792-82), rat anti-Ki67-Alexa Fluor 660 (1:100, ThermoFisher, 50-5698-82), rabbit anti-Iba1 (1:400, FujiFilm Wako, 019-19741), rat anti-CD68-Alexa Fluor 700 (1:50, BioRad, MCA1957A700), rat anti-Ter119-Super Bright 436 (1:100, ThermoFisher, 62-5921-82) and goat anti-CD45 (1:200, R&D Systems, AF114) diluted in the blocking solution overnight at 4 °C. After three 5-min washes in PBS with 0.5% Tween-20, the sections were incubated with donkey anti-goat-Alexa Fluor 647 (1:500, Invitrogen, A21447), donkey anti-rabbit-Alexa Fluor 405 (1:1,000, ThermoFisher, A48258), donkey anti-rabbit-Alexa Fluor 488 (1:1,000, Abcam, ab150073) and donkey anti-goat-Alexa Fluor 405 (1:1,000, Abcam, ab175664) and diluted in the blocking solution for 2 h at r.t. SMA was labelled with Alexa Fluor 488-conjugated 1A4 monoclonal antibody (1:500, Thermo-Fisher, 53-9760-82). Sections were imaged with a Leica Stellaris 5 confocal microscope (Leica Microsystems). Images were processed with Fiji/ImageJ. Coronal sections from brains of CCM mice ($n = 4$) with lesions and surrounding brain tissue exposed to PCD-modulated FUS-MB treatment 30 days earlier were stained with hematoxylin and eosin (H&E). Individual H&E sections with CCMs present in both FUS-MB-treated and contralateral control hemispheres were identified. Images of these sections, with at least one section per mouse in the group, were sent to a neuropathologist (J.W.M.) for observation.

Analysis of immunofluorescence images

Images were collected as a *z*-stack of 1-µm step size at either ×20 or ×63 magnification. For ×20 images, tiled images were collected to cover the perilesional and intralesional space of sonicated and non-sonicated CCMs. For ×63 images, non-tiled images were acquired along the perilesional and intralesional boundary of sonicated and non-sonicated lesions. Maximum intensity projections were produced in Fiji/ImageJ. Quantification of cell markers, morphology and co-localization was conducted in HALO using the object co-localization and highplex modules, except that co-localization of SMA and *Krit1*[KO] endothelium was performed using the 'Colocalization' plugin for ImageJ.

Statistical analyses

The '*n*' values per group are made evident either by individual datapoints shown or statement of '*n*' values in figures, figure legends and/or manuscript text. Statistical significance was assessed at $P < 0.05$ for all experiments. Linear mixed-effect models were conducted and analysed with the lme4 package (v.1.1.34) and the emmeans package (v.1.8.9) in R Studio. All other statistical tests were performed using GraphPad Prism 9. Statistical tests, models and *P* values are listed in detail for all manuscript figures in Supplementary Table 2.

Reporting summary

Further information on research design is available in the Nature Portfolio Reporting Summary linked to this article.

Data availability

The data supporting the results in this study are available within the paper and its Supplementary Information. Source data are provided with this paper. MRIs from these studies are available on UVA Dataverse at https://doi.org/10.18130/V3/SAVMVD (ref. 78). Source data for the figures are provided with this paper.

References

1. Snellings, D. A. et al. Cerebral cavernous malformation: from mechanism to therapy. *Circ. Res.* **129**, 195–215 (2021).
2. Detter, M. R., Snellings, D. A. & Marchuk, D. A. Cerebral cavernous malformations develop through clonal expansion of mutant endothelial cells. *Circ. Res.* **123**, 1143–1151 (2018).
3. Tanriover, G. et al. Ultrastructural analysis of vascular features in cerebral cavernous malformations. *Clin. Neurol. Neurosurg.* **115**, 438–444 (2013).
4. Wei, S. et al. Cerebral cavernous malformation proteins in barrier maintenance and regulation. *Int. J. Mol. Sci.* **21**, 675 (2020).
5. Peyre, M. et al. Somatic PIK3CA mutations in sporadic cerebral cavernous malformations. *N. Engl. J. Med.* **385**, 996–1004 (2021).
6. Ren, A. A. et al. PIK3CA and CCM mutations fuel cavernomas through a cancer-like mechanism. *Nature* **594**, 271–276 (2021).
7. Zabramski, J. M. et al. The natural history of familial cavernous malformations: results of an ongoing study. *J. Neurosurg.* **80**, 422–432 (1994).
8. Awad, I. A. & Polster, S. P. Cavernous angiomas: deconstructing a neurosurgical disease. *J. Neurosurg.* **131**, 1–13 (2019).
9. Garcia, R. M., Oh, T., Cole, T. S., Hendricks, B. K. & Lawton, M. T. Recurrent brainstem cavernous malformations following primary resection: blind spots, fine lines, and the right-angle method. *J. Neurosurg.* **135**, 671–682 (2020).
10. Dammann, P. et al. Surgical treatment of brainstem cavernous malformations: an international Delphi consensus. *J. Neurosurg.* **136**, 1220–1230 (2022).
11. Dumot, C. et al. Stereotactic radiosurgery for haemorrhagic cerebral cavernous malformation: a multi-institutional, retrospective study. *Stroke Vasc. Neurol.* **9**, 221–229 (2024).
12. Akers, A. et al. Synopsis of guidelines for the clinical management of cerebral cavernous malformations: consensus recommendations based on systematic literature review by the Angioma Alliance Scientific Advisory Board Clinical Experts Panel. *Neurosurgery* **80**, 665–680 (2017).
13. Flemming, K. D. & Lanzino, G. Cerebral cavernous malformation: what a practicing clinician should know. *Mayo Clin. Proc.* **95**, 2005–2020 (2020).
14. Girard, R. et al. Plasma biomarkers of inflammation and angiogenesis predict cerebral cavernous malformation symptomatic hemorrhage or lesional growth. *Circ. Res.* **122**, 1716–1721 (2018).
15. Hart, B. L., Taheri, S., Rosenberg, G. A. & Morrison, L. A. Dynamic contrast-enhanced MRI evaluation of cerebral cavernous malformations. *Transl. Stroke Res.* **4**, 500–506 (2013).
16. White, E. et al. *2022 State of the Field Report* (Focused Ultrasound Foundation, 2022).
17. Meng, Y. et al. Safety and efficacy of focused ultrasound induced blood-brain barrier opening, an integrative review of animal and human studies. *J. Control. Release* **309**, 25–36 (2019).
18. Bérard, C. et al. Anticancer drug delivery by focused ultrasound-mediated blood-brain/tumor barrier disruption for glioma therapy: from benchside to bedside. *Pharmacol. Ther.* **250**, 108518 (2023).
19. Gorick, C. M. et al. Applications of focused ultrasound-mediated blood-brain barrier opening. *Adv. Drug Deliv. Rev.* **191**, 114583 (2022).
20. Fisher, D. G. & Price, R. J. Recent advances in the use of focused ultrasound for magnetic resonance image-guided therapeutic nanoparticle delivery to the central nervous system. *Front. Pharmacol.* **10**, 1348 (2019).
21. Timbie, K. F., Mead, B. P. & Price, R. J. Drug and gene delivery across the blood-brain barrier with focused ultrasound. *J. Control. Release* **219**, 61–75 (2015).
22. Leinenga, G. & Götz, J. Scanning ultrasound removes amyloid-β and restores memory in an Alzheimer's disease mouse model. *Sci. Transl. Med.* **7**, 278ra33 (2015).
23. Schaeffer, V. et al. Stimulation of autophagy reduces neurodegeneration in a mouse model of human tauopathy. *Brain* **135**, 2169–2177 (2012).
24. Lee, Y. et al. Improvement of glymphatic–lymphatic drainage of beta-amyloid by focused ultrasound in Alzheimer's disease model. *Sci. Rep.* **10**, 16144 (2020).
25. Jordão, J. F. et al. Amyloid-β plaque reduction, endogenous antibody delivery and glial activation by brain-targeted, transcranial focused ultrasound. *Exp. Neurol.* **248**, 16–29 (2013).
26. Leinenga, G., Koh, W. K. & Götz, J. Scanning ultrasound in the absence of blood-brain barrier opening is not sufficient to clear β-amyloid plaques in the APP23 mouse model of Alzheimer's disease. *Brain Res. Bull.* **153**, 8–14 (2019).
27. Todd, N. et al. Secondary effects on brain physiology caused by focused ultrasound-mediated disruption of the blood–brain barrier. *J. Control. Release* **324**, 450–459 (2020).
28. Chernaya, O. et al. Biomechanics of endothelial tubule formation differentially modulated by cerebral cavernous malformation proteins. *iScience* **9**, 347 (2018).
29. Stockton, R. A., Shenkar, R., Awad, I. A. & Ginsberg, M. H. Cerebral cavernous malformations proteins inhibit Rho kinase to stabilize vascular integrity. *J. Exp. Med.* **207**, 881–896 (2010).
30. Mleynek, T. M. et al. Lack of CCM1 induces hypersprouting and impairs response to flow. *Hum. Mol. Genet.* **23**, 6223–6234 (2014).
31. Novell, A. et al. A new safety index based on intrapulse monitoring of ultra-harmonic cavitation during ultrasound-induced blood-brain barrier opening procedures. *Sci. Rep.* **10**, 10088 (2020).

32. Haqshenas, S. R. & Saffari, N. Multi-resolution analysis of passive cavitation detector signals. *J. Phys. Conf. Ser.* **581**, 012004 (2015).

33. Chien, C. Y., Xu, L., Pacia, C. P., Yue, Y. & Chen, H. Blood–brain barrier opening in a large animal model using closed-loop microbubble cavitation-based feedback control of focused ultrasound sonication. *Sci. Rep.* **12**, 16147 (2022).

34. O'Reilly, M. A. & Hynynen, K. Blood-brain barrier: real-time feedback-controlled focused ultrasound disruption by using an acoustic emissions-based controller. *Radiology* **263**, 96–106 (2012).

35. Abrahao, A. et al. First-in-human trial of blood–brain barrier opening in amyotrophic lateral sclerosis using MR-guided focused ultrasound. *Nat. Commun.* **10**, 4373 (2019).

36. Mehta, R. I. et al. Blood-brain barrier opening with MRI-guided focused ultrasound elicits meningeal venous permeability in humans with early Alzheimer disease. *Radiology* **298**, 654–662 (2021).

37. Mead, B. P. et al. Focused ultrasound preconditioning for augmented nanoparticle penetration and efficacy in the central nervous system. *Small* **15**, e1903460 (2019).

38. O'reilly, M. A., Hough, O. & Hynynen, K. Blood-brain barrier closure time after controlled ultrasound-induced opening is independent of opening volume. *J. Ultrasound Med.* **36**, 475–483 (2017).

39. Marty, B. et al. Dynamic study of blood-brain barrier closure after its disruption using ultrasound: a quantitative analysis. *J. Cereb. Blood Flow Metab.* **32**, 1948–1958 (2012).

40. Mainprize, T. et al. Blood-brain barrier opening in primary brain tumors with non-invasive MR-guided focused ultrasound: a clinical safety and feasibility study. *Sci. Rep.* **9**, 321 (2019).

41. Gasca-Salas, C. et al. Blood-brain barrier opening with focused ultrasound in Parkinson's disease dementia. *Nat. Commun.* **12**, 779 (2021).

42. Lipsman, N. et al. Blood–brain barrier opening in Alzheimer's disease using MR-guided focused ultrasound. *Nat. Commun.* **9**, 2336 (2018).

43. Fisher, D. G. et al. Magnetic resonance imaging of mouse cerebral cavernomas reveal differential lesion progression and variable permeability to gadolinium. *Arterioscler. Thromb. Vasc. Biol.* **43**, 958–970 (2023).

44. Gee, J. M. et al. Imaging activity in neurons and glia with a Polr2a-based and cre-dependent GCaMP5G-IRES-tdTomato reporter mouse. *Neuron* **83**, 1058–1072 (2014).

45. Malinverno, M. et al. Endothelial cell clonal expansion in the development of cerebral cavernous malformations. *Nat. Commun.* **10**, 2761 (2019).

46. Kline-Schoder, A. R. et al. Characterization of the responses of brain macrophages to focused ultrasound-mediated blood–brain barrier opening. *Nat. Biomed. Eng.* **8**, 650–663 (2024).

47. Grewal, S. et al. Using focused ultrasound to modulate microglial structure and function. *Front. Cell. Neurosci.* **17**, 1290628 (2023).

48. Baumgartner, J. E. et al. Pathologically proven cavernous angiomas of the brain following radiation therapy for pediatric brain tumors. *Pediatr. Neurosurg.* **39**, 201–207 (2003).

49. Novelli, P. M., Reigel, D. H., Gleason, P. L. & Yunis, E. Multiple cavernous angiomas after high-dose whole-brain radiation therapy. *Pediatr. Neurosurg.* **26**, 322–325 (1997).

50. Pollock, B. E. et al. Stereotactic radiosurgery of cavernous malformations. *J. Neurosurg.* **93**, 987–991 (2000).

51. Flemming, K. D. & Lanzino, G. Stereotactic radiosurgery for cavernous malformations: natural history or treatment effect? *Neurology* **93**, 921–922 (2019).

52. Martínez-Lage, J. F. et al. Cavernomas in children with brain tumors: a late complication of radiotherapy. *Neurocirugia* **19**, 50–54 (2008).

53. Koike, T. et al. High incidence of radiation-induced cavernous hemangioma in long-term survivors who underwent hematopoietic stem cell transplantation with radiation therapy during childhood or adolescence. *Biol. Blood Marrow Transplant.* **18**, 1090–1098 (2012).

54. Vinchon, M. et al. Radiation-induced tumors in children irradiated for brain tumor: a longitudinal study. *Childs Nerv. Syst.* **27**, 445–453 (2011).

55. Strenger, V. et al. Intracerebral cavernous hemangioma after cranial irradiation in childhood: incidence and risk factors. *Strahlenther. Onkol.* **184**, 276–280 (2008).

56. Burn, S., Gunny, R., Phipps, K., Gaze, M. & Hayward, R. Incidence of cavernoma development in children after radiotherapy for brain tumors. *J. Neurosurg. Pediatr.* **106**, 379–383 (2007).

57. Jain, R. et al. Radiation-induced cavernomas of the brain. *Am. J. Neuroradiol.* **26**, 1158–1162 (2005).

58. Heckl, S., Aschoff, A. & Kunze, S. Radiation-induced cavernous hemangiomas of the brain. *Cancer* **94**, 3285–3291 (2002).

59. Cutsforth-Gregory, J. K., Lanzino, G., Link, M. J., Brown, R. D. & Flemming, K. D. Characterization of radiation-induced cavernous malformations and comparison with a nonradiation cavernous malformation cohort. *J. Neurosurg.* **122**, 1214–1222 (2015).

60. Globisch, M. A., Onyeogaziri, F. C., Smith, R. O., Arce, M. & Magnusson, P. U. Dysregulated hemostasis and immuno-thrombosis in cerebral cavernous malformations. *Int. J. Mol. Sci.* **23**, 12575 (2022).

61. Tung, Y.-S., Vlachos, F., Feshitan, J. A., Borden, M. A. & Konofagou, E. E. The mechanism of interaction between focused ultrasound and microbubbles in blood-brain barrier opening in mice. *J. Acoust. Soc. Am.* **130**, 3059–3067 (2011).

62. Choi, J. J. et al. Microbubble-size dependence of focused ultrasound-induced blood–brain barrier opening in mice in vivo. *IEEE Trans. Biomed. Eng.* **57**, 145 (2010).

63. Tsai, C. H., Zhang, J. W., Liao, Y. Y. & Liu, H. L. Real-time monitoring of focused ultrasound blood-brain barrier opening via subharmonic acoustic emission detection: implementation of confocal dual-frequency piezoelectric transducers. *Phys. Med. Biol.* **61**, 2926–2946 (2016).

64. Tos, S. M., Mantziaris, G., Shaaban, A. & Sheehan, J. P. Stereotactic radiosurgery for intracranial cavernous malformations of the deep-seated locations: systematic review and meta-analysis. *Neurosurg. Rev.* **47**, 186 (2024).

65. Yousefi, O., Sabahi, M., Malcolm, J., Adada, B. & Borghei-Razavi, H. Laser interstitial thermal therapy for cavernous malformations: a systematic review. *Front. Surg.* **9**, 887329 (2022).

66. Munier, S. M., Liang, A. S., Desai, A. N., James, J. K. & Danish, S. F. Characterization of magnetic resonance thermal imaging signal artifact during magnetic resonance guided laser-induced thermal therapy. *Oper. Neurosurg.* **19**, 619–624 (2020).

67. Polster, S. P. et al. Trial readiness in cavernous angiomas with symptomatic hemorrhage (CASH). *Neurosurgery* **84**, 954–964 (2019).

68. Polster, S. P. et al. Atorvastatin treatment of cavernous angiomas with symptomatic hemorrhage exploratory proof of concept (AT CASH EPOC) trial. *Neurosurgery* **85**, 843–853 (2019).

69. Girard, R. et al. Vascular permeability and iron deposition biomarkers in longitudinal follow-up of cerebral cavernous malformations. *J. Neurosurg.* **127**, 102–110 (2016).

70. Alcazar-Felix, R. J. et al. Except for robust outliers, rapamycin increases lesion burden in a murine model of cerebral cavernous malformations. *Transl. Stroke Res.* https://doi.org/10.1007/s12975-024-01270-9 (2024).

71. Mathew, A. S. S. et al. Single-cell mapping of focused ultrasound-transfected brain. *Gene Ther.* **30**, 255–263 (2023).

72. Poon, C., Pellow, C. & Hynynen, K. Neutrophil recruitment and leukocyte response following focused ultrasound and microbubble mediated blood-brain barrier treatments. *Theranostics* **11**, 1655 (2021).

73. Sheybani, N. D. et al. Profiling of the immune landscape in murine glioblastoma following blood brain/tumor barrier disruption with MR image-guided focused ultrasound. *J. Neurooncol.* **156**, 109–122 (2022).

74. Curley, C. T. et al. Immunomodulation of intracranial melanoma in response to blood-tumor barrier opening with focused ultrasound. *Theranostics* **10**, 8821–8833 (2020).

75. Curley, C. T., Sheybani, N. D., Bullock, T. N. & Price, R. J. Focused ultrasound immunotherapy for central nervous system pathologies: challenges and opportunities. *Theranostics* **7**, 3608–3623 (2017).

76. Rezai, A. R. et al. Ultrasound blood–brain barrier opening and aducanumab in Alzheimer's disease. *N. Engl. J. Med.* **390**, 55–62 (2024).

77. Burke, C. W. et al. Markedly enhanced skeletal muscle transfection achieved by the ultrasound-targeted delivery of non-viral gene nanocarriers with microbubbles. *J. Control. Release* **162**, 414–421 (2012).

78. Price, R. MRIs for: Focused ultrasound-microbubble treatment arrests the growth and formation of cerebral cavernous malformations. *UVA Dataverse* https://doi.org/10.18130/V3/SAVMVD (2024).

Acknowledgements

Author contributions

D.G.F. and R.J.P. conceptualized the study. D.G.F. conducted the experiments with the aid of C.M.G., V.R.B., A.C.D., M.R.H. and T.C. in animal preparation and MRI acquisition. MRI sequences were optimized by G.W.M. P.T. developed the CCM model with genetic tracing *Krit1* null cells, and K.A.S. generated the experimental animals with assistance from D.G.F. and T.C. Longitudinal MRI data were acquired by D.G.F. and analysed by D.G.F. and I.M.S. D.G.F. and K.A.S. performed immunostaining and confocal imaging with technical guidance from J.D.S. and J.R.L. J.W.M. analysed histology images. J.P.S. and D.S. provided SRS clinical treatment plans, and D.M. provided FUS-MB clinical treatment plans. D.G.F. and R.J.P. designed the figures and wrote the manuscript. J.D.S., A.C.D., J.S.P., J.R.L., P.T., G.W.M. and R.J.P. edited the manuscript. All authors approved the manuscript.

Competing interests

The authors declare no competing interests.

Additional information

Supplementary information The online version contains supplementary material available at https://doi.org/10.1038/s41551-025-01390-z.

Correspondence and requests for materials should be addressed to Petr Tvrdik or Richard J. Price.

Peer review information *Nature Biomedical Engineering* thanks the anonymous reviewers for their contribution to the peer review of this work. Peer reviewer reports are available.

Reprints and permissions information is available at www.nature.com/reprints.

Publisher's note Springer Nature remains neutral with regard to jurisdictional claims in published maps and institutional affiliations.

Corresponding author(s): Richard J Price

Last updated by author(s): Mar 26, 2025

Reporting Summary

Nature Portfolio wishes to improve the reproducibility of the work that we publish. This form provides structure for consistency and transparency in reporting. For further information on Nature Portfolio policies, see our Editorial Policies and the Editorial Policy Checklist.

Statistics

For all statistical analyses, confirm that the following items are present in the figure legend, table legend, main text, or Methods section.

n/a	Confirmed	
☐	☒	The exact sample size (*n*) for each experimental group/condition, given as a discrete number and unit of measurement
☐	☒	A statement on whether measurements were taken from distinct samples or whether the same sample was measured repeatedly
☐	☒	The statistical test(s) used AND whether they are one- or two-sided *Only common tests should be described solely by name; describe more complex techniques in the Methods section.*
☐	☒	A description of all covariates tested
☐	☒	A description of any assumptions or corrections, such as tests of normality and adjustment for multiple comparisons
☐	☒	A full description of the statistical parameters including central tendency (e.g. means) or other basic estimates (e.g. regression coefficient) AND variation (e.g. standard deviation) or associated estimates of uncertainty (e.g. confidence intervals)
☐	☒	For null hypothesis testing, the test statistic (e.g. *F*, *t*, *r*) with confidence intervals, effect sizes, degrees of freedom and *P* value noted *Give P values as exact values whenever suitable.*
☒	☐	For Bayesian analysis, information on the choice of priors and Markov chain Monte Carlo settings
☒	☐	For hierarchical and complex designs, identification of the appropriate level for tests and full reporting of outcomes
☒	☐	Estimates of effect sizes (e.g. Cohen's *d*, Pearson's *r*), indicating how they were calculated

Our web collection on statistics for biologists contains articles on many of the points above.

Software and code

Policy information about availability of computer code

Data collection	MR images were collected with Siemens IDEA (VB17) at 7T and with Bruker Paravison (3.2) at 9T. Focused ultrasound was performed and acoustic emissions collect with FUS Instruments Aureus RK300 BBB. Immunofluorescent images were collected with Leica Leica Application Suite X (4.6.1.27508).
Data analysis	Emissions data was processed and spectrograms were generated with MATLAB (9.14). Edema and hemosiderin deposition in lesion-free brain tissue following FUS BBBO were evaluated with 3D Slicer (5.2). Gadolinium accumulation following FUS BBBO was evaluated using the enhancement of T1 contrast in T1-RARE images with Horos DICOM viewer (4.0.0RC4). CCM volume prior to, and longitudinally following, FUS BBBO was evaluated in Horos using the high resolution T2-weighted spin echo MR images. Immunfluorescence images were processed with Fiji/ImageJ (version 1.54). Quantification of cell markers, morphology, and colocalization was conducted in HALO (3.6) using the Object Colocalization and Highplex modules. Linear mixed effect models were conducted and analyzed with the lme4 package (version 1.1.34) and the emmeans package (version 1.8.9) with R (4.3.1) in R Studio (2023.09.0+463). All other statistical tests were performed using GraphPad Prism 9 (San Diego, USA). Statistical tests, models, and p-values are listed in detail for all manuscript figures in Table S2.

For manuscripts utilizing custom algorithms or software that are central to the research but not yet described in published literature, software must be made available to editors and reviewers. We strongly encourage code deposition in a community repository (e.g. GitHub). See the Nature Portfolio guidelines for submitting code & software for further information.

Data

All manuscripts must include a data availability statement. This statement should provide the following information, where applicable:

- Accession codes, unique identifiers, or web links for publicly available datasets
- A description of any restrictions on data availability
- For clinical datasets or third party data, please ensure that the statement adheres to our policy

> The data supporting the results in this study are available within the paper and its Supplementary Information. Source data for the figures are provided with this paper. MRIs from these studies are provided at https://doi.org/10.18130/V3/SAVMVD.

Research involving human participants, their data, or biological material

Policy information about studies with human participants or human data. See also policy information about sex, gender (identity/presentation), and sexual orientation and race, ethnicity and racism.

Reporting on sex and gender	N/A
Reporting on race, ethnicity, or other socially relevant groupings	N/A
Population characteristics	N/A
Recruitment	N/A
Ethics oversight	N/A

Note that full information on the approval of the study protocol must also be provided in the manuscript.

Field-specific reporting

Please select the one below that is the best fit for your research. If you are not sure, read the appropriate sections before making your selection.

☒ Life sciences ☐ Behavioural & social sciences ☐ Ecological, evolutionary & environmental sciences

For a reference copy of the document with all sections, see nature.com/documents/nr-reporting-summary-flat.pdf

Life sciences study design

All studies must disclose on these points even when the disclosure is negative.

Sample size	Sample sizes were not calculated, but were largely dictated by litter sizes and availability of Krit1 null mice, as well as the number of CCMs present per hemisphere in each individual Krit1 null mouse. Sample sizes are provided for each and every figure in the manuscript. Comprehensive details on statistical tests used, p-values, variance, standard deviations, and standard errors are provided in Table S2.
Data exclusions	No data were excluded from the study
Replication	The findings of focused ultrasound blood-brain barrier opening-induced control of lesion volume were replicated across 3 distinct cohorts of mice ranging across 9 litters and utilizing both sexes with 3 different focused ultrasound regimens. All tested cohorts and regimens were successful in controlling lesion growth.
Randomization	All mice in this study received focused ultrasound sonication. Cavernomas within mice that met the selection criteria for sonication were randomly assigned for sonication or no sonication.
Blinding	During data collection, investigators were not blinded to group allocations as cavernomas assigned for sonication must be physically selected for targeting in the FUS instruments Aureus RK300 software. During data analysis, investigators not present for data collection analyzed MR images and were blinded to sonication status. These analyses were reviewed and combined with analysis performed by an investigator who was not blinded to sonication status to ensure correct treatment assignment and uniformity of analysis. For IF analysis, a set algorithm in HALO was applied uniformly to images of either treatment assignment.

Reporting for specific materials, systems and methods

We require information from authors about some types of materials, experimental systems and methods used in many studies. Here, indicate whether each material, system or method listed is relevant to your study. If you are not sure if a list item applies to your research, read the appropriate section before selecting a response.

Materials & experimental systems

n/a	Involved in the study
☐	☒ Antibodies
☒	☐ Eukaryotic cell lines
☒	☐ Palaeontology and archaeology
☐	☒ Animals and other organisms
☒	☐ Clinical data
☒	☐ Dual use research of concern
☒	☐ Plants

Methods

n/a	Involved in the study
☒	☐ ChIP-seq
☒	☐ Flow cytometry
☐	☒ MRI-based neuroimaging

Antibodies

Antibodies used	Anti-CD31 (1:20, R&D Systems, AF3628), rat anti-GFAP-Alexa Fluor 488 (1:50, eBioscience, 53-9792-82), rat anti-Ki67-Alexa Fluor 660 (1:100, ThermoFisher, 50-5698-82), rabbit anti-Iba1 (1:400, FujiFilm Wako, 019-19741), rat anti-CD68-Alexa Fluor 700 (1:50, BioRad, MCA1957A700), rat anti-Ter119-Super Bright 436 (1:100, ThermoFisher, 62-5921-82), goat anti-CD45 (1:200, R&D Systems, AF114), donkey anti-goat-Alexa Fluor 647 (1:500, Invitrogen A21447), donkey anti-rabbit-Alexa Fluor 405 (1:1000, ThermoFisher, A48258), donkey anti-rabbit-Alexa Fluor 488 (1:1000, Abcam, ab150073), and donkey anti-goat-Alexa Fluor 405 (1:1000, Abcam, ab175664). Alpha-smooth muscle actin (SMA) was labeled with Alexa Fluor™ 488 conjugated 1A4 monoclonal antibody (1:500, ThermoFisher, 53-9760-82).
Validation	All antibodies used for IF in this study were validated by the manufacturer and/or had citations for the correct species (mouse) and application (IF).

Animals and other research organisms

Policy information about studies involving animals; ARRIVE guidelines recommended for reporting animal research, and Sex and Gender in Research

Laboratory animals	Mouse sex, litter, age, and treatment assignment are listed in detail in Table S1. Mice were housed in a temperature range of 65-75°F (18-23°C) and humidity levels of 40-60%. To generate the CCM murine models (Pdgfb-CreERT2;Krit1fl/null or Cdh5-CreERT2;Krit1fl/null), Pdgfb-CreERT2 or Cdh5-CreERT2 mice were crossed with Krit1fl/null male or females. On postnatal day 5, Krit1 gene ablation was induced with an injection of tamoxifen (subcutaneous; 50uL at 2mg/mL in corn oil). Genotypes were confirmed using Transnetyx (Cordova, TN). Control mice in this study were C57BL/6; Charles River. Mice were treated between 9 and 13 weeks of age.
Wild animals	Study did not involve wild animals.
Reporting on sex	Both sexes were studied. Sex diaggregated data are provided in Figure S4.
Field-collected samples	Study did not involve samples collected in the field.
Ethics oversight	All animal experiments were approved by the University of Virginia Animal Care and Use Committee.

Note that full information on the approval of the study protocol must also be provided in the manuscript.

Plants

Seed stocks	N/A
Novel plant genotypes	N/A
Authentication	N/A

Magnetic resonance imaging

Experimental design

Design type	Resting state

Design specifications	Following baseline MR image acquisition, images were reviewed to assess appropriate CCMs for sonication. CCMs located within the left or right caudoputamen, corpus callosum, or cerebral cortex were eligible for targeting.
Behavioral performance measures	N/A

Acquisition

Imaging type(s)	Structural. T1 contrast and T2-weighted spin echo.
Field strength	7T and 9.4T
Sequence & imaging parameters	MR imaging was performed using either a 7T Bruker/Siemens ClinScan or a 9.4T Bruker BioSpec small animal MRI scanner. T2-weighted spin echo images were acquired at 7T with the Siemens 3D T2-SPACE sequence (repetition time of 3000 ms, echo time of 80 ms, pixel size of 125 μm x 125 μm x 100 μm, 2 averages, and 20 min acquisition time) or at 9.4T with the Bruker 3D T2-TurboRARE sequence (repetition time of 2000 ms, echo time of 55 ms, turbo factor of 18, pixel size of 125 μm x 125 μm x 125 μm, 1 average, and 30 min acquisition time). Susceptibility-weighted images were acquired only at 7T (repetition time of 18 ms, echo time of 10 ms, pixel size of 130 μm x 130 μm x 130 μm, 2 averages, and 15 min acquisition time). T1-weighted spin echo images were acquired at 9.4T with the Bruker 2D T1-RARE sequence (repetition time of 1500 ms, echo time of 6 ms, pixel size of 156 μm x 156 μm x 350 μm, 1 average, and 3 min acquisition time). All imaging was performed under isoflurane anesthesia, and body temperature was maintained with a heated, circulating water bed.
Area of acquisition	Whole brain scans
Diffusion MRI	☐ Used ☒ Not used

Preprocessing

Preprocessing software	Bias field correction was performed in 3D Slicer (5.2) using N4ITK MRI Bias Field Correction filter with manually segmented brain mask.
Normalization	N/A
Normalization template	N/A
Noise and artifact removal	N/A
Volume censoring	N/A

Statistical modeling & inference

Model type and settings	Statistical tests, models, and p-values are listed in detail for all manuscript figures in Table S2. Linear mixed effects model by restricted maximum likelihood was performed with random effects of mouse ID and lesion ID and fixed effects of treatment condition, time point, and starting lesion volume.
Effect(s) tested	Effect of focused ultrasound-mediated blood-brain barrier opening or no sonication on lesion volume was tested. Linear mixed effect model as described above was used followed by pairwise differences of treatment condition and time point interaction with Tukey's p-value adjustment for a family of 6 estimates. See Table S2 for more details.

Specify type of analysis: ☐ Whole brain   ☒ ROI-based   ☐ Both

Anatomical location(s)	ROIs were manually segmented for sonicated cavernomas and contralateral cavernomas. Cavernomas were manually segmented around their hypointense boundaries. Sonicated brain regions were identified by hyperintense focal column of blood-brain barrier opening and gadolinium delivery in T1 contrast images.

Statistic type for inference	N/A

(See [Eklund et al. 2016](#))

Correction	Pairwise differences of treatment condition and time point interaction were evaluated with Tukey's p-value adjustment for a family of estimates.

Models & analysis

n/a	Involved in the study
☒	Functional and/or effective connectivity
☒	Graph analysis
☒	Multivariate modeling or predictive analysis